

Anomaly detection in the Zwicky Transient Facility DR3

K. L. Malanchev,^{1,2}★ M. V. Pruzhinskaya,² V. S. Korolev,^{3,4} P. D. Aleo,^{1,5}
 M. V. Kornilov,^{2,6} E. E. O. Ishida,⁷ V. V. Krushinsky,⁸ F. Mondon,⁷ S. Sreejith,^{7,11}
 A. A. Volnova,⁹ A. A. Belinski,² A. V. Dodin,² A. M. Tatarnikov² and S. G. Zheltoukhov^{2,10}
 (The SNAD Team)

¹Department of Astronomy, University of Illinois at Urbana-Champaign, 1002 West Green Street, Urbana, IL 61801, USA

²Lomonosov Moscow State University, Sternberg Astronomical Institute, Universitetsky pr. 13, Moscow, 119234, Russia

³Central Aerohydrodynamic Institute, 1 Zhukovsky st, Zhukovsky, Moscow Region, 140180, Russia

⁴Moscow Institute of Physics and Technology, 9 Institutskiy per., Dolgoprudny, Moscow Region, 141701, Russia

⁵Center for Astrophysical Surveys Fellow, National Center for Supercomputing Applications, USA

⁶National Research University Higher School of Economics, 21/4 Staraya Basmannaya Ulitsa, Moscow, 105066, Russia

⁷Université Clermont Auvergne, CNRS/IN2P3, LPC, F-63000 Clermont-Ferrand, France

⁸Laboratory of Astrochemical Research, Ural Federal University, Ekaterinburg, Russia, ul. Mira d. 19, Yekaterinburg, Russia, 620002

⁹Space Research Institute of the Russian Academy of Sciences (IKI), 84/32 Profsoyuznaya Street, Moscow, 117997, Russia

¹⁰Faculty of Physics, Lomonosov Moscow State University, Leninskie Gory 1-2, 119991 Moscow, Russia

¹¹Physics Department, Brookhaven National Laboratory, Upton, NY 11973

Accepted XXX. Received YYY; in original form ZZZ

ABSTRACT

We present results from applying the SNAD anomaly detection pipeline to the third public data release of the Zwicky Transient Facility (ZTF DR3). The pipeline is composed of 3 stages: feature extraction, search of outliers with machine learning algorithms and anomaly identification with followup by human experts. Our analysis concentrates in three ZTF fields, comprising more than 2.25 million objects. A set of 4 automatic learning algorithms was used to identify 277 outliers, which were subsequently scrutinised by an expert. From these, 188 (68%) were found to be bogus light curves – including effects from the image subtraction pipeline as well as overlapping between a star and a known asteroid, 66 (24%) were previously reported sources whereas 23 (8%) correspond to non-catalogued objects, with the two latter cases of potential scientific interest (e. g. 1 spectroscopically confirmed RS Canum Venaticorum star, 4 supernovae candidates, 1 red dwarf flare). Moreover, using results from the expert analysis, we were able to identify a simple bi-dimensional relation which can be used to aid filtering potentially bogus light curves in future studies. We provide a complete list of objects with potential scientific application so they can be further scrutinised by the community. These results confirm the importance of combining automatic machine learning algorithms with domain knowledge in the construction of recommendation systems for astronomy. Our code is publicly available†.

Key words: methods: data analysis – stars: variables: general – transients: supernovae – astronomical data bases: miscellaneous

1 INTRODUCTION

The meaning of astronomical discovery has changed throughout history, but it has always been highly correlated with the technological development of the era and the sociological construct which accompanies it. In astronomy, the discovery of new or unexpected astronomical sources was often serendipitous (Dick 2013), for ex-

ample, the discovery of gamma-ray bursts in the late 1960s by the Vela satellites (Klebesadel et al. 1973) or the discovery of the cosmic microwave background radiation by Robert Wilson and Arno Penzias (Penzias & Wilson 1965). The advent of the CCD highly increased our ability to gather photometric data, and allowed programmed systematic searches for scientifically interesting objects (Perlmutter et al. 1992; Filippenko 1992; Richmond et al. 1993). Nevertheless, manual screening continued to play a central role in the discovery of new sources (e. g. Cardamone et al. 2009; Borisov 2019).

★ E-mail: kostya@illinois.edu

† <https://github.com/snad-space/zwad>

The arrival of large scale sky surveys like the Sloan Digital Sky Survey (SDSS; Blanton et al. 2017) and, more recently, the Zwicky Transient Facility (ZTF; Bellm et al. 2019; Masci et al. 2019) pushed this paradigm even further. Confronted with data sets holding observational data from around a billion sources, the use of automated machine learning methods to search for new physics was unavoidable (Ball & Brunner 2010). This trend, shifting the astronomical data analysis towards data-driven approaches, is highly recognised in supervised learning tasks (e.g. photometric classification of transients, Ishida 2019), but it is as crucial for unsupervised ones. Given that new astronomical surveys are always accompanied by technological developments which allow them to probe different epochs in the evolution of the Universe, or different regions within our own galaxy, every new instrument has a high probability of observing previously non-catalogued phenomena. At the same time, every new data set is more complex and bigger than its precedents. In the absence of appropriate unsupervised learning pipelines, we may miss the discovery opportunity which is in the root of all scientific endeavour.

This key aspect of unsupervised learning in astronomical research has been recognised by the research community with some extent, producing interesting illustrative examples: Rebbapragada et al. (2009) discovered periodic variable stars using a Phased k -means algorithm; Hoyle et al. (2015) isolated and removed problematic objects for photometric redshift estimation with an Elliptical Envelope routine; Nun et al. (2016) selected five different algorithms for an ensemble method tested on three MACHO fields and confirmed some objects belonging to rare classes; Baron & Poznanski (2017) identified anomalous galaxy spectra based on an Unsupervised Random Forest (URF); Solarz et al. (2017) used One-Class Support Vector Machine (O-SVM) to find weird objects in photometric data, including a few misclassifications; Reyes & Estévez (2020) used a geometric transformation-based model to highlight artefacts' properties from real objects in ZTF images; and Soraisam et al. (2020, 2021) identified novel events in variable source population by computing distributions of magnitude changes over time intervals for a given filter.

The task of applying machine learning algorithms to real data also requires the data to be translated into an acceptable format for automatic learning applications, for example each light curve could be transformed to a vector of features. Modern astronomical data are frequently composed of a large number of correlated features which must be simplified and/or homogenised. Several works provide details on efforts in the dimensionality reduction stage. For example: Pruzhinskaya et al. (2019) located both novel and misclassified transient events light curves in the Open Supernova Catalog (Guillochon et al. 2017) after applying t-SNE to Gaussian-process approximated light curves, combined with an isolation forest (IF) and confirmed by expert analysis. Martínez-Galarza et al. (2020) implemented tree-based algorithms (IF, URF) and two manifold-based algorithms (t-SNE, UMAP) to identify anomalies, using their *bona fide* anomaly Boyajian's star (KIC 8462852, Boyajian et al. 2016) as reference, and investigated how an ensemble of such methods can be used to find objects of similar phenomenology or astrophysical characteristics. This work was built off of Giles & Walkowicz (2019), who used t-SNE to visually represent cluster membership designations of Kepler light curve data (including Boyajian's star as a "ground truth" anomaly) from DBSCAN. The same authors applied the same technique to range *Kepler* objects by their outlier score (Giles & Walkowicz 2020). Similarly, Webb et al. (2020) used t-SNE to visually represent HDBSCAN cluster membership designations of *Deeper, Wider, Faster program* light curves combined

with anomaly scores assigned by an IF algorithm in their interactive ASTRONOMY package (Lochner & Bassett 2020).

In this work we present detailed description of a complete anomaly detection pipeline and its results when applied to three fields from ZTF Data Release 3 (DR3)¹. The SNAD² pipeline was built with the goal of exploiting the potential of modern astronomical data sets for discovery and under the hypothesis that, although automatic learning algorithms have a crucial role to play in this task, the scientific discovery is only completely realised when such systems are designed to boost the impact of domain knowledge experts. Our approach combines a diverse set of machine learning algorithms, tailored feature extraction procedures and domain knowledge experts who validate the results of the machine learning pipeline (Pruzhinskaya et al. 2019; Kornilov et al. 2019; Ishida et al. 2019; Malanchev et al. 2020; Aleo et al. 2020).

In what follows, Section 2 describes the ZTF data and the adopted preprocessing steps. Section 3 details the outlier detection algorithms, followup observations and expert analysis employed in this work. Section 4 lists the outliers found by the complete pipeline and Section 5 reports numerical efficiency of our pipeline in identifying fake light curves. Section 6 provides a deeper analysis of our feature parameter space. Our conclusions are outlined in Section 7. We also provide further details of our analysis in the appendices: Appendix A mathematically defines the extracted light curve features, and Appendix B describes the SNAD ZTF DR object web-viewer and cross-match tool, constructed to help the experts in their critical evaluation of each outlier. Appendix C illustrates results from the light curve fit of the supernova candidates and Appendix D lists properties of each anomaly candidate discovered from this work.

Our code, *zwad*, is publicly available at <https://github.com/snad-space/zwad>, and the SNAD team's ZTF DR3 object viewer can be found at <https://ztf.snad.space/>.

2 ZTF DATA

The Zwicky Transient Facility is a 48-inch Schmidt telescope on Mount Palomar, equipped with a 47 deg² camera, which allows rapid scanning of the entire north sky. The ZTF survey started on March 2018 and during its initial phase has observed around a billion objects (Bellm et al. 2019). Beyond representing the current state of the art in rapid photometric observations, ZTF also has the crucial role of being the predecessor of the next generation of large scale surveys like the Vera Rubin Observatory Legacy Survey of Space and Time³ (LSST). Many of its data protocols are being used as test-bench for LSST systems.

In this work, we analysed data from the first 9.4 months of the ZTF survey, between 17 March and 31 December 2018 ($58194 \leq \text{MJD} \leq 58483$). This period includes data from ZTF private survey, thus having a better cadence than the rest of DR3. We selected only perfectly clean extractions at every epoch (`catflag = 0`) obtained in passband z_r , which encloses more than half of all objects.

Light curves from ZTF DR3 are spread over 1020 fields, with objects within the same field being sampled with a similar cadence — on average ~ 1 day for the Galactic plane and ~ 3 days for the Northern-equatorial sky. In order to minimise effects due to different cadences, we performed our analysis in three separate

¹ <https://www.ztf.caltech.edu/page/dr3>

² <https://snad.space>

³ <https://www.lsst.org/>

fields: “M31” (a part of ZTF field 695), which includes the Andromeda galaxy (Messier 1781), “DEEP” (ZTF field 795), located far from the galactic plane, and “DISK” (ZTF field 805), located in the Galaxy plane. The Andromeda galaxy region is a well-studied part of the sky, thus allowing further scrutiny of candidates with external information. The Andromeda galaxy is fully imaged by only one CCD, thus the M31 field of view (FOV) is only 1/16 of ZTF light-sensitive area ($\sim 3 \text{ deg}^2$), and does not contain as many objects as the two other fields. For DISK and DEEP, we chose fields with high declination, which allow easier follow-up observations by northern hemisphere facilities, and which maximise the number of field objects.

We imposed a final selection cut by choosing light curves with at least 100 observations in M31 and DEEP, and at least 500 observations in DISK. All data were downloaded from IRSA IPAC⁴. The number of light curves passed through the selection cuts are shown in Table 1 along with a few other properties of these fields.

3 METHODOLOGY

Our anomaly detection pipeline is composed of 3 stages: feature extraction (Section 3.1), outlier detection using machine learning (Section 3.2) and domain expert analysis (Section 3.3).

We consider as outliers all the objects which result from the machine learning algorithms. Among the outliers we define two groups of objects, i. e. “bogus outliers” and “anomaly candidates”. To the former case, we assign all artefacts of image processing, bad columns on CCDs, tracks from satellites, diffraction spikes and other cases of non-astrophysical variability. To the latter case, we attribute the objects whose variability is proved to be astrophysically real and related either to the internal properties of the source or to the environmental effects, e. g. present of a companion. All the anomaly candidates have a potential to be interesting for the experts in the corresponding domain. If after thorough expert-investigation an object is shown to behave unusually for its suspected astrophysical type, has unknown nature of variability, or represents a rare class of objects, then we deem it an “anomaly”. It has to be stressed that the experts can miss some anomalies from the anomaly candidates due to insufficient knowledge in a particular domain of variable stars or transients or the lack of opportunity to perform the additional observations with required facilities. Therefore, presenting the results of this work in Table D, we show not only anomalies confirmed by us, but the other anomaly candidates that have a potential to be proved as anomalies by other experts in the field.

All light-curve data sets were submitted to the same feature extraction procedure before being used as input to different machine learning algorithms.

3.1 Feature extraction

We extracted 42 features from each light curve. Some of them probe magnitude properties (e. g. Amplitude, Von Neumann η , Standard Deviation), while others are specific summary statistics for periodic signals (e. g. Periodogram Amplitude, Periodogram η , Periodogram Standard Deviation). This ensemble of features describe different aspects of the light curve shape, with the tails of feature distributions indicating objects with less common light curves properties, or potential outliers. A detailed description of each feature is given

in Appendix A. Light-curve feature data within each field were standardised by shifting to zero mean and re-scaling to unity standard deviation. This ensures the results from outlier detection strategies will not depend on the units of the input variables.

3.2 Outlier detection algorithms

This section describes the outlier detection algorithms used in this study, which are aimed to select objects located in sparse regions of the feature space. Our pipeline profits from the Python `scikit-learn` (Pedregosa et al. 2011) implementation for all strategies.

3.2.1 Isolation Forest

Isolation Forest is an unsupervised outlier detection algorithm first proposed by Liu et al. (2008). It considers that outliers are normally isolated from nominal data in the input parameter space, hence requiring less number of random partitions to be separated from it. Its scores are based on the inverse distance from root to leaf node in an ensemble of decision trees built with random split points. Outliers are identified as objects with shorter path length from root to leaf node and the score is inversely proportional to the average path root-to-leaf among all trees in the forest.

The two main parameters that describe an IF are: the number of trees and the sub-sample size used to train each tree. In what follows all results were obtained using sub-samples of 1000 elements and a forest containing 1000 trees.

3.2.2 Local Outlier Factor

The Local Outlier Factor (LOF, Breunig et al. 2000) algorithm detects outliers in a data set based on comparative local density estimation. For each object in the data set, its local density is calculated using the distance between the object and its k -th nearest neighbour and the total number of neighbours it encloses (k). The average local density is calculated over all k neighbours and the score is defined as the ratio between the individual and average local densities. Normal objects are expected to have similar local density to that of its neighbours, while outliers will show significant differences.

The behaviour of the LOF algorithm is dictated by two main parameters: the number of neighbours k and the metric used to calculate the distance between instances. The number of neighbours, k , in particular is an important criterion, since too high a value of k might cause the algorithm to miss outliers while too small a value results in a narrow focus which might be especially problematic in the case of noisy datasets. In what follows, all results were obtained using $k = 100$ with the distances given by the Euclidean metric.

3.2.3 Gaussian Mixture Model

A Gaussian Mixture Model (GMM, McLachlan & Peel 2000) is a parametric description of the data which assumes that multiple classes can be modelled as a superposition of multivariate Gaussian distributions. An object is considered to belong to a group according to its probability of being generated by one of the Gaussians within the model. Alternatively, an outlier is defined as an object for which all Gaussians within the mixture assign a low probability. The most important variable that defines the GMM is the number

⁴ https://irsa.ipac.caltech.edu/data/ZTF/lc_dr3/

Table 1. Properties of three ZTF fields analysed in this work.

Field name	ZTF field	Centre (α , δ)	Centre (l , b)	FOV	N	Object count
M31	Field 695, ccdid 11	10 ^h 72, 41 ^m 34	121 ^o 20, -21 ^o 51	3 deg ²	≥ 100	57 546
DEEP	Field 795	246 ^h 72, 54 ^m 88	83 ^o 91, 42 ^o 45	55 deg ²	≥ 100	406 611
DISK	Field 807	19 ^h 99, 62 ^m 05	126 ^o 27, -0 ^o 63	55 deg ²	≥ 500	1 790 565

of components, or groups, to consider. In what follows, we used 10 isotropic Gaussian components.

3.2.4 One-class Support Vector Machines

Support Vector Machines (Cristianini et al. 2000; Hastie et al. 2009) were originally formulated to tackle supervised binary classification scenarios. This is achieved by defining a hyperplane which separates points belonging to different classes. If the different classes are not linearly separable in a given feature space, they are projected into a higher dimensional feature space where they can be linearly separated using a kernel (‘kernel trick’). Schölkopf et al. (1999) proposed a modification to this method for novelty/outlier detection called One-class SVM. Analogously to its supervised learning counterpart, O-SVM identifies a decision boundary, by defining the smallest hypersphere containing the bulk part of the data. The model has two parameters: ν , often called the margin which defines the probability of finding a new but normal point outside the decision boundary, and the kernel. In this work we used $\nu = 0.01$ and a Gaussian radial basis function kernel.

3.3 Domain expert analysis

Outlier detection algorithms are, in general, able to identify statistical abnormalities within a large data set, e. g. objects from sparse regions of the feature space or which do not conform with the general statistical description of the data. However, these may not be of astrophysical interest. Our approach to mining scientifically significant peculiarities admits that the light curve itself is typically not enough to determine the scientific content of a given source. Therefore, each outlier automatically identified is subjected to analysis by a human expert with the goal of scrutinising its characteristics and determining the degree of its astrophysical content. In this context, all automatic learning algorithms can be seen as recommendation systems whose goal is to perform a first triage which is subsequently confirmed by a human. The expert analysis includes literature and community search, cross-matching with known databases and catalogues, analysis of compatibility with theoretical models and, when possible, additional photometric and/or spectroscopic observations. The final aim of the last stage is identification of anomalies (scientifically interesting objects confirmed by the expert) from outliers (candidates identified with high scores by the machine learning algorithms).

3.3.1 The ZTF viewer

In order to provide a smooth experience for the experts in charge of analysing outliers, we constructed a specially designed web-interface which allows smooth visualisation of several light curve characteristics: the SNAD ZTF viewer⁵ (Fig. B1). It enables easy access to the individual exposure images; to the Aladin Sky Atlas (Bonnarel et al. 2000; Boch & Fernique 2014) and to various

catalogues of variable stars and transients, including the General Catalogue of Variable Stars (GCVS, Samus’ et al. 2017), the American Association of Variable Star Observers’ Variable Star Index (AAVSO VSX, Watson et al. 2006), the Asteroid Terrestrial-impact Last Alert System (ATLAS, Heinze et al. 2018), the ZTF Catalog of Periodic Variable Stars (Chen et al. 2020), astrocats⁶, the OGLE-III On-line Catalog of Variable Stars (Soszynski et al. 2008), and the SIMBAD database (Wenger et al. 2000).

In ZTF DR3 each OID corresponds to an object in a particular field and passband, therefore the same source can have several OIDs. Our viewer allows the user to perform fast coordinate cross-match to associate a given OID with others from different fields and passbands, under a user-defined cross-match radius. Full description of the SNAD ZTF viewer is given in Appendix B.

3.3.2 Additional observations

For a few anomaly candidates we also performed additional observations with the telescopes at the Caucasus Mountain Observatory which belongs to the Sternberg Astronomical Institute, Lomonosov Moscow State University (CMO SAI MSU, Shatsky et al. 2020).

Photometric observations were carried with the 60-cm Ritchie-Chretien telescope in g' , r' , i' passbands (Fukugita et al. 1996), in remote control mode (RC600, Berdnikov et al. 2020). Photometric reductions were performed using standard methods of dark frames and twilight sky flat-fields. Fluxes were extracted with the aperture photometry technique using fixed aperture radius ≈ 2.5 full width at half maximum (FWHM) of the stellar point spread function of the frame. We used an ensemble of 400 nearby stars from Pan-STARRS DR1 catalogue (Chambers et al. 2016; Flewelling et al. 2016) to derive the linear solution between instrumental and Pan-STARRS DR1 magnitudes. Some stars were ejected from ensemble due to 3σ -clipping. The final number of comparison stars in each ensemble was ~ 200 – 300 for different objects.

Spectra were obtained with the Transient Double-beam Spectrograph (TDS) of the 2.5-meter telescope (Potanin et al. 2017). The general characteristics of the TDS and the data reduction methods are described in Potanin et al. (2020). The slit was oriented vertically in order to reduce wavelength dependent slit losses caused by atmospheric dispersion. The wavelength calibration was performed with a Ne-Al-Si lamp and corrected by using night-sky emission lines that allowed us to achieve an accuracy of $\lesssim 10 \text{ km s}^{-1}$. The spectra were extracted with an aperture of 4.5 arcsec. The flux calibration was performed by dividing the extracted spectra by the response curve, calculated with the spectrophotometric standard BD+28d4211. However, the photometric accuracy was lost due to the narrow slit, which was used to achieve a higher spectral resolution. Barycentric radial velocity corrections were applied.

⁵ <https://ztf.snad.space/>

⁶ <https://astrocats.space/>

4 RESULTS

We applied the outlier detection algorithms separately to each field. M31 and DEEP fields were scrutinised by all four algorithms, while for DISK we used only IF, GMM and O-SVM (LOF had a prohibitively high computation cost given the number of objects in this field). For all machine learning algorithms, the 40 objects with largest values of outlier score were submitted to the expert analysis. Taking into account that a few objects were assigned high anomaly scores by more than one algorithm, the final list of unique outliers contained 277 objects: 101 in M31, 113 in DEEP and 63 in DISK. Each one of the 277 was subjected to the expert analysis using the utilities described in Section 3.3. A summary of the properties describing anomaly candidates is given in Table D1. The first column is the object identifier from ZTF DR3. The second column contains alternative nomenclature by which the object is known. The equatorial coordinates (α , δ) in degrees are presented in the 3rd column. The 4th and 5th columns show the minimum and maximum zr magnitudes derived from the entire public light curve of ZTF DR3. The line-of-sight reddening in our galaxy $E(B - V)$ is given in column 6 (Schlafly & Finkbeiner 2011). The 7th column indicates the distance to the object (D) in parsec according to Bailer-Jones et al. (2018); for objects belonging to M31 we adopt a distance of ~ 780 kpc (Makarov et al. 2014). The 8th column gives the approximate absolute zr magnitude derived as $M_{r,\max} = m_{r,\max} - 5 \log_{10} D + 5 - A_r$, where A_r is the Milky Way foreground absorption in zr passband. Column 9 contains the best period P_0 , in days, extracted from either the Lomb–Scargle periodogram (see Appendix A) or one of the catalogues listed in the ZTF-viewer or determined by us. In case of previously catalogued objects, their types and the source of classification are listed in columns 10 and 11, respectively.

4.1 M31

Among the 101 outliers automatically identified in the M31 field there are 80 bogus light curves and 21 objects of astrophysical nature, 7 of which are not listed in known catalogues and/or databases of variable sources. As expected, a large part of anomaly candidates in this field belongs to the M31 galaxy. Further information about these objects is given in Table D1.

The known variables from our list are distributed by types as follows: 3 classical Cepheids (M31), 2 red supergiants (RSG, M31), 1 eclipsing binary (EB, MW), 2 possible novae (PNV, M31), 1 RS Canum Venaticorum-type binary system (RSCVN, MW), and 5 objects of unknown nature of variability.

4.1.1 695211200019653 — RSCVN

The object 695211200019653 (Fig. 1) was previously classified as a star with sine-like variability and period $P = 7.696$ d in the ATLAS catalog of variable stars (Heinze et al. 2018). The ASAS-SN Catalog of Variable Stars (Jayasinghe et al. 2020) classifies it as a rotation variable with $P = 7.709$ d and the ZTF Catalog of Periodic Variable Stars (Chen et al. 2020) considers it a RSCVN with period $P = 7.734$ d based on an automatic DBSCAN classifier. Moreover, this object is also marked as X-ray and UV source by ROSAT, XMM-Newton and Swift/UVOT. According to the Gaia DR2 (Gaia Collaboration et al. 2018), it is a Milky Way object at the distance $D \approx 1640$ pc, $R \approx 2.34 R_\odot$, $T_{\text{eff}} \approx 4500$ K, and $L \approx 2 L_\odot$.

Its ZTF DR3 light curves are characterised by amplitude variability, e. g. around MJD $\approx 58750 - 58850$ when the minimums

become deeper. Moreover, its zg light curve shows two observations at MJD ≈ 58368.4 which could be a flare with an amplitude of $\gtrsim 0.1$ mag. The Transiting Exoplanet Survey Satellite (TESS, Ricker et al. 2014) observed 695211200019653 continuously during ~ 3 periods. Its light curve shows an asymmetric sine-like variability with amplitude of $\approx 3\%$, significant inter-period changing (typical for stars with spot activity) and ~ 0.05 mag flare near MJD ≈ 58779.5 . The estimated period is 7.662 d. The difference in periods estimation from different surveys can be explained by the low signal to noise ratio of ASAS-SN data, irregular sampling of ZTF and ATLAS data, and by the short observation sequence of TESS. Alternatively, the difference could also be explained by a real fluctuation in period due to changing of positions and temperatures of stellar spots.

We obtained two spectra of 695211200019653 with a resolution of ~ 1500 and a signal to noise ratio of ~ 50 on 2020 August 22 and November 12 (MJD = 59083.9651 and MJD = 59165.7250) with a 1 arcsec slit and total exposure times of 1500 s and 1800 s, correspondingly (see Fig. 2). Spectral classification was done by comparing with the spectral library (Valdes et al. 2004). We determined the spectral class as K3. Strong variable Balmer and Ca II H-K emissions are present in all spectra, indicating chromospheric activity (Wilson 1968). Velocities of the emission lines correspond to the absorption lines. The radial velocity shift between two spectra is 46 ± 10 km s $^{-1}$, that points out to the presence of a second companion. However, we did not detect any obvious spectral signs of a companion in the spectra. Based on overall analysis, distance estimation, photometric and spectral data we definitely classified 695211200019653 as RS Canum Venaticorum-type binary system (Berdyugina 2005).

4.1.2 695211200075348 — Unclassified Variable

The object M31N 2013-11b was first discovered by Ovcharov et al. (2013) on 2013 Nov. 7.780 UT (MJD = 56603.780) with $R \approx 20.3$ mag and classified as probable nova in M31. Later on, 2013 Nov.-Dec., Hornoch (2013) observed the object using the 0.65-m telescope at Ondrejov and the Danish 1.54-m telescope at La Silla. The observations revealed a significant red colour which is not typical for a classical nova unless the object is highly reddened, which is not expected for its line of sight. Hornoch (2013) concluded that it is more likely a red long-period variable which is supported also by its very slow brightening.

On MJD = 57633.1234 MASTER-IAC auto-detection system discovered the optical transient source, MASTER OT J004126.22+414350.0, at the same position with unfiltered magnitude ~ 19.7 mag (Shumkov et al. 2016). Williams et al. (2016) performed spectroscopic and additional photometric observations with the 2-m Liverpool Telescope on 2016 Sep 9 UT. The spectrum revealed no obvious emission or absorption lines, but the continuum was clearly detected. Spectroscopic and photometric observations of the transient implied it is unlikely to be a recurrent nova eruption in M31. The colour of the transient also suggests it is unlikely to be a Galactic dwarf nova outburst. The ZTF object light curve is given in Fig. 3.

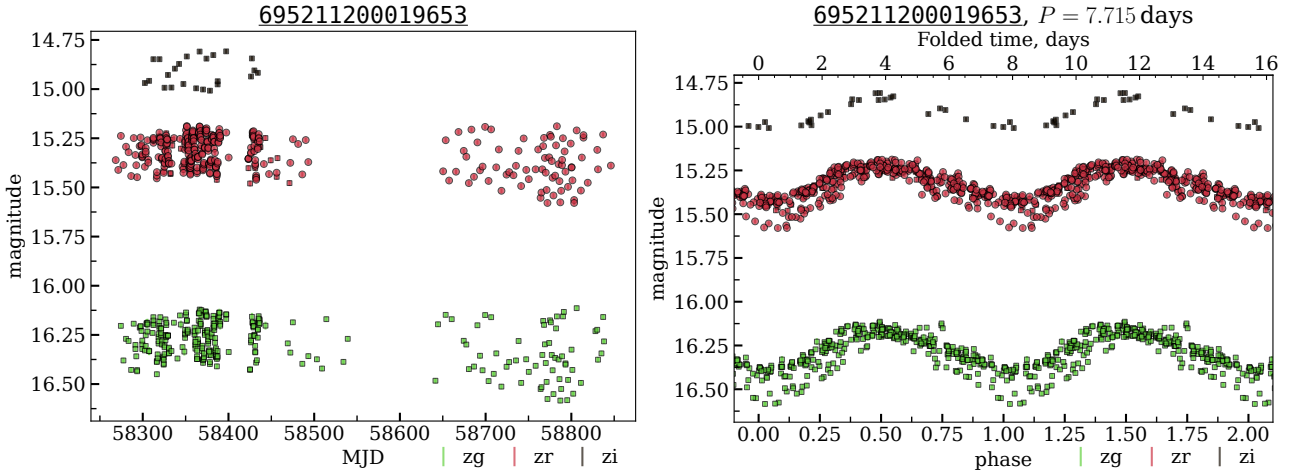


Figure 1. The light curve of RS Canum Venaticorum-type variable. **Left:** observed ZTF light curve. **Right:** folded light curve using $P = 7.715$ d obtained using our feature extraction code (see Appendix A). Note the minimum depth change after $\text{MJD} \geq 58750$ (left) and the two outlier zg observations in the folded light curve (right). OIDs: 695111200008124, 695211200019653, 695311200027644, 1735101200013615, 1735201200018614. Different colours denote the different ZTF passbands. Red circles correspond to the outlier OID, squares show data from other OIDs corresponding to the same source but found in different passbands and ZTF fields.

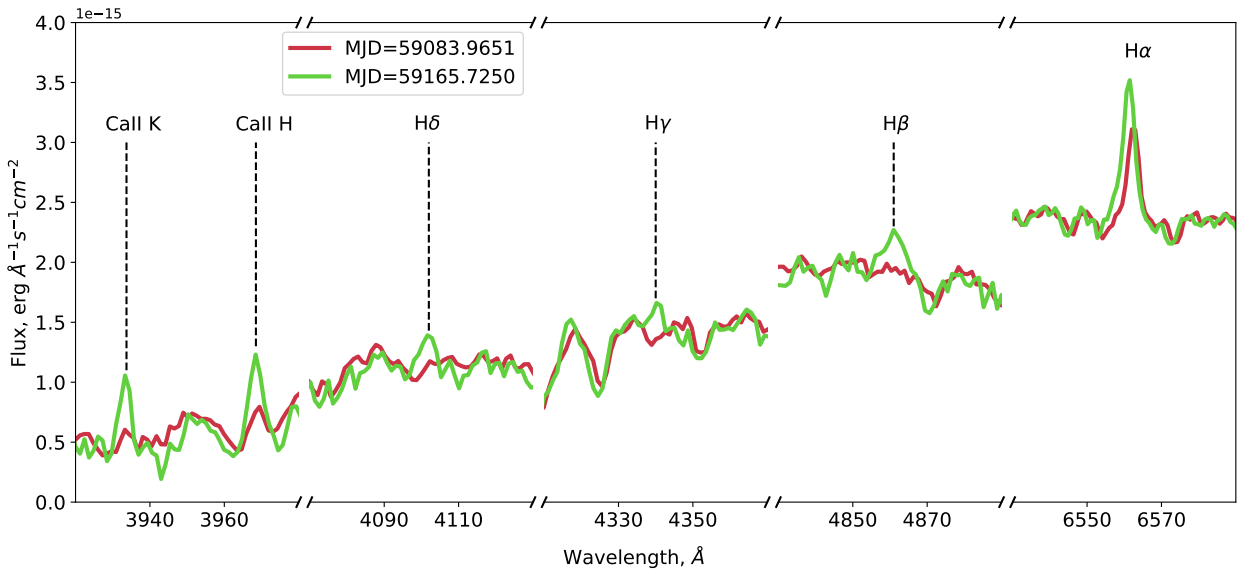


Figure 2. Ca II H-K and Balmer series emissions on two spectra of 695211200019653 obtained with the 2.5-meter telescope of CMO SAI MSU.

4.1.3 695211100022045 — Nova Candidate

According to the Transient Name Server⁷ (TNS), the object 695211100022045 was first seen on 2017-10-29 (MJD = 58055) as AT 2017ixs. It was detected a second time on 2017-12-15 (MJD = 58102) with 19.5 mag in Clear filter and classified as a possible nova (Carey 2017) in M 31. Six months later, on 2018-06-20 (MJD = 58289), MASTER-Kislovodsk auto-detection system discovered MASTER OT J004355.89+413209.9 with an unfiltered magnitude of 19.0 mag at AT 2017ixs position (Balanutsa et al. 2018). The behaviour of its light curve is not typical for a dwarf nova or a cat-

aclysmic variable, therefore, AT 2017ixs is the interesting anomaly for the further study. The ZTF object light curve is given in Fig. 4.

4.1.4 695211100131796 — LBV Candidate

The object 695211100131796 (Fig. 5) is located near the ionised hydrogen region [AMB2011] HII 2692 (Azimlu et al. 2011). It was previously detected as an object of unknown nature PSO J011.0457+41.5548 (Lee et al. 2014). Based on the spectra of PSO J011.0457+41.5548, which is turned to be typical of B- and A-type supergiants, Humphreys et al. (2017) concluded that the available information is insufficient to confirm it as a luminous blue variable

⁷ <https://www.wis-tns.org>

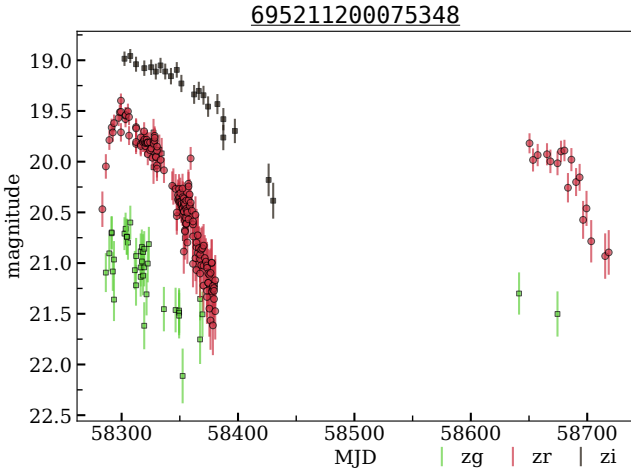


Figure 3. The light curves of M31N 2013-11b/MASTER OT J004126.22+414350.0 — unclassified variable object from the M31 field. OIDs: 695111200015523, 695211200075348, 695311200020148, 1735101200009309, 1735201200040725.

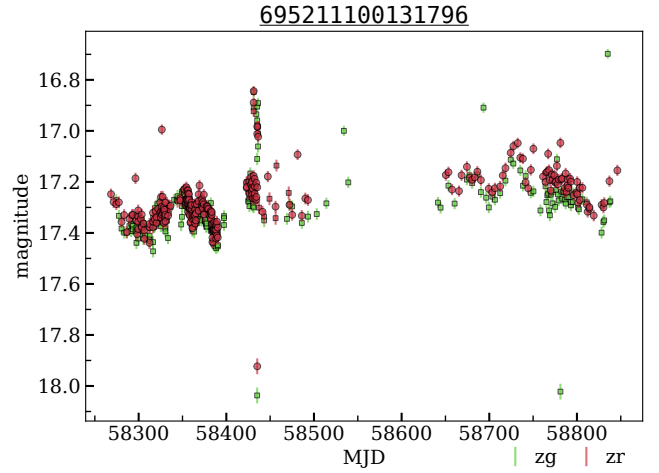


Figure 5. The light curves of PSO J011.0457+41.5548 — luminous blue variable candidate from the M31 field. OIDs: 695111100014264, 695211100131796, 1735101200058759, 1735201200018887.

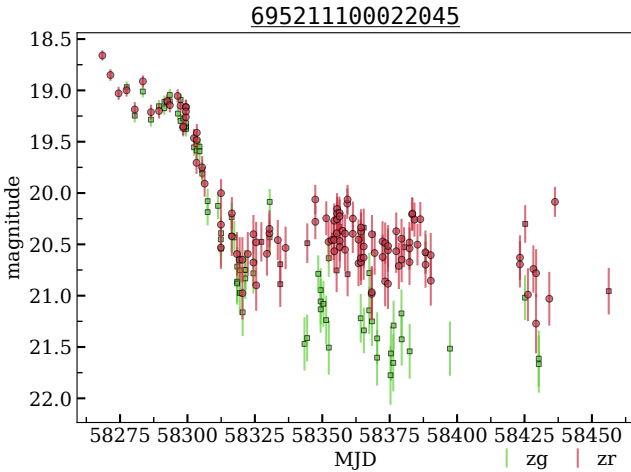


Figure 4. The light curves of AT 2017ixs/MASTER OT J004355.89+413209.9 — nova candidate from the M31 field. OIDs: 695111100031492, 695211100022045, 1735101200034700, 1735201200049286.

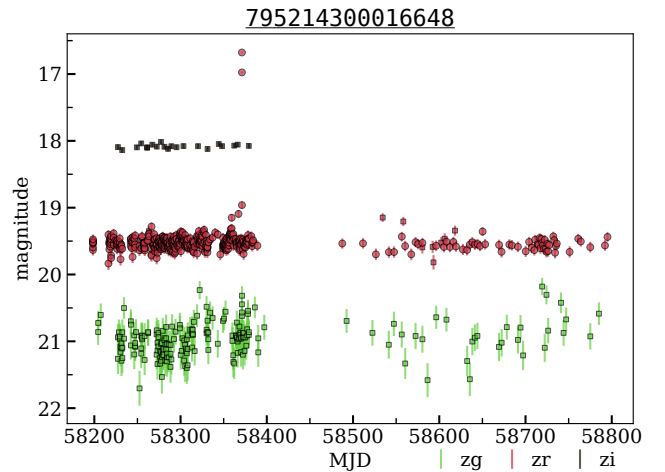


Figure 6. The light curves of 795214300016648 from the DEEP field classified by us as red dwarf flare. OIDs: 795114300008349, 795214300016648, 795314300011499, 1829206200019338.

(LBV). We consider it a luminous blue variable or variable of the S Doradus type (SDOR) candidate.

4.2 DEEP

Among the 113 outliers in the DEEP field there are 95 bogus light curves and 18 objects of astrophysical nature, 8 of which are not listed in known catalogues and/or databases of variable sources. The information about these objects is given in Table D1.

The known variables from our list are distributed by types as follows: 2 eclipsing binaries, 2 semi-regular variables, 1 Mira variable, 1 RR Lyrae variable with asymmetric light curve (steep ascending branches), 1 polar, 1 Type Ia Supernova (SN), 2 supernova candidates.

4.2.1 795214300016648 — Red Dwarf Flare

Among the unclassified objects we would like to mention, 795214300016648 is a possible red dwarf flare (Fig. 6). It is a relatively nearby object at a distance of ~ 400 pc (Bailer-Jones et al. 2018), with a high proper motion $PM_{R.A.} = 8.122 \pm 0.502$ mas/yr, $PM_{Dec.} = -29.269 \pm 0.596$ mas/yr (Gaia Collaboration et al. 2018). Despite the fact that such objects are quite common in our galaxy, their detection is rare because of the small duration and low luminosity of its flares. Their study is of great scientific interest due to the potential habitability associated to the planets it hosts (e. g. Segura et al. 2010; France et al. 2013).

4.2.2 Supernova Candidates

In the outlier list from DEEP there are 6 objects that are possibly of extragalactic origin — 795202100005941, 795204100013041, 795205100007271, 795209200003484, 795212100007964, 795213200000671. Two of them appeared in the databases as known supernova candidates: 795213200000671 (AT 2018afz/Gaia18apj⁸) and 795202100005941 (MLS180307:163438+521642; Drake et al. 2009). Considering the photometric redshift of the possible host galaxy, 795202100005941 absolute magnitude is ~ -22.4 , making it a potential superluminous supernova (SLSN) candidate. The four remaining objects are not catalogued.

We use the PYTHON library SNCOSMO⁹ to fit their light curves with several supernova models: Peter Nugent’s spectral templates¹⁰ which cover the main supernova types (Ia, Ib/c, IIP, IIL, IIn) and SALT2 model of Type Ia Supernovae (Guy et al. 2007). Each model is characterised by a set of parameters. Nugent’s models are the simple spectral time series that can be scaled up and down. The parameters of the models are the redshift z , the observer-frame time corresponding to the zero source’s phase, t_0 , and the amplitude. The zero phase is defined relative to the explosion moment and the observed time t is related to phase via $t = t_0 + \text{phase} \times (1 + z)$.

The SALT2 model is more sophisticated and contains the parameters that affect the shape of the spectrum at each phase. In addition to the redshift, t_0 , and amplitude, the light curves are also characterised by x_1 (stretch) and c (colour) parameters. The x_1 parameter describes the time-stretching of the light curve. The c parameter corresponds to the colour offset with respect to the average at the date of maximum luminosity in B -band, i. e. $c = (B - V)_{\text{max}} - \langle B - V \rangle$. In SALT2 models the zero phase is defined relative to the maximum in B -band.

For each object we extracted photometry in zg, zr, zi passbands from DEEP field only. In a few cases, due to insufficient number of photometrical points in zi , we added to the zi -light curve observations from other fields. Then, we subtracted the reference magnitude from ZTF light curves to roughly account for the host galaxy contamination. In order to perform the fit, we determined the redshift bounds for each supernova candidate. For three objects (see Table 2) there are known SDSS galaxies at the source position with measured photometric redshift with errors, which we used for the redshift bounds. For the remaining ones, we adopted $[-15; -22]$ as an acceptable region for the supernovae absolute magnitude (Richardson et al. 2014) and, then, using the apparent maximum magnitude, roughly transform it to the possible redshift range.

Since dust in the Galaxy also affects the shape of an observed spectrum, we accounted for it as an additional effect during the fitting procedure. We used Cardelli et al. (1989) extinction model and the individual object’s colour excess $E(B - V)$ (see Table D1).

Results from the light curve fit are presented in Fig. C1, C2, C3, C4. We do not show the fitted light curves for 795202100005941, 795213200000671 since both supernova candidates were discovered after the maximum light and only descending part of the light curves is available. The analysis of four non-catalogued supernova candidates revealed that their light curves are similar to those of Type Ia Supernovae. The determined x_1 and

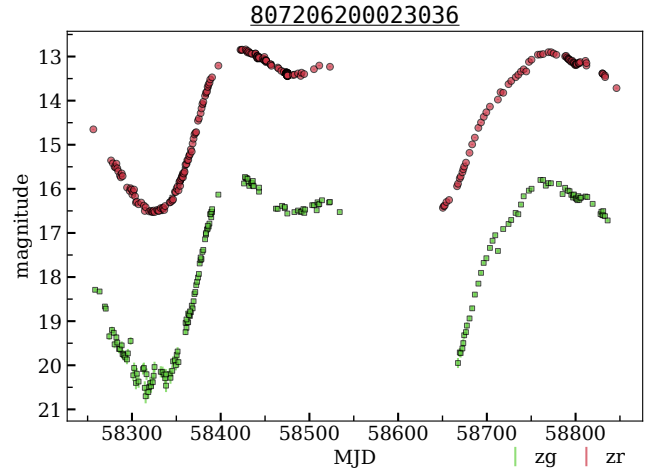


Figure 7. The light curves of NSVS J0122238+611352 — Mira variable from the Disk field. OIDs: 807106200016307, 807206200023036, 1810114300003360, 1810214300006290.

c parameters are typical for SNe Ia. We summarised the main parameters using the SALT2 model in Table 2.

4.3 Disk

Among the 63 outliers in the Disk field there are 13 bogus light curves and 50 variable objects of astrophysical nature, 8 of which are not listed in known catalogues and/or databases of variable sources. The information about these objects is given in Table D1.

Among the known variables from our list there are 3 dwarf novae, 5 eclipsing systems, 1 Orion variable with rapid light variations, 28 Mira variables, 1 other long-period variable of unspecified type and 4 candidates to pre-main-sequence (PMS) stars. These objects are considered anomaly candidates, and therefore, interesting sources to study more carefully. For example, some of these Mira variables have asymmetric light curves which may indicate the presence of a companion (e. g. 807206200023036, Fig. 7).

4.3.1 Pre-main-sequence candidates

We identified four objects (807206200003542, 807206200004116, 807206200014645, 807210200026027) previously classified as pre-main-sequence candidates (Vioque et al. 2020). For these objects, we gathered additional observations with the RC600 telescope of CMO SAI MSU in g', r', i' passbands (Table 3) and confirmed that the variability is still present. Three of them are located at a distance of 800–1000 pc, and the last one (807210200026027) is significantly further, at 1700 pc (Bailer-Jones et al. 2018). In particular, 807210200026027 can be also found among the AGN candidates reported by Edelson & Malkan (2012). In order to identify AGN candidates, Edelson & Malkan (2012) used the colour information from the Wide-field Infrared Survey Explorer (WISE; Wright et al. 2010), the Two Micron All-Sky Survey (2MASS; Skrutskie et al. 2006), and checked their presence in X-rays data with ROSAT All-Sky Survey (RASS; Voges et al. 1999). However, 807210200026027 was assigned as an AGN solely based on infrared observations, making it a weak candidate, and in contradiction with Gaia parallax (Gaia Collaboration et al. 2018). Based on ML techniques, the object was also classified as a

⁸ <http://gsaweb.ast.cam.ac.uk/alerts/home>

⁹ <https://sncosmo.readthedocs.io/en/stable/>

¹⁰ https://c3.lbl.gov/nugent/nugent_templates.html

Table 2. Results of the light curve fit with the SALT2 model for supernova candidates from the DEEP field.

OID	Host galaxy*	z_{ph}	z	t_0	x_1	c	Comments [†]
795202100005941/ZTF18aanbnjh	SDSS J163437.92+521642.2	0.424 ± 0.103	—	—	—	—	Blazar
795204100013041/ZTF18abgvctp	SDSS J160913.83+521251.3	0.375 ± 0.138	~ -0.24	58320.9336 ± 0.4389	1.71 ± 0.51	-0.044 ± 0.035	—
795205100007271/ZTF18aatjtf	—	—	~ -0.20	58285.8334 ± 0.1810	-0.54 ± 0.18	-0.075 ± 0.021	SN Ia
795209200003484/ZTF18abbpebf	—	—	~ -0.11	58299.7269 ± 0.0008	0.60 ± 0.12	-0.013 ± 0.012	SN Ia
795212100007964/ZTF18aanbksg	SDSS J161144.90+555740.7	0.288 ± 0.122	~ -0.18	58214.4470 ± 0.0002	0.40 ± 0.20	-0.282 ± 0.020	Blazar
795213200000671/ZTF18aainciv	—	—	—	—	—	—	AGN-I

* If available, candidate host galaxies from SDSS DR16 (Ahumada et al. 2020) and their corresponding photometric redshifts (z_{ph} , obtained via the KD-tree method).

[†] According to the light curve classifier of the ALeRCE broker (Förster et al. 2020).

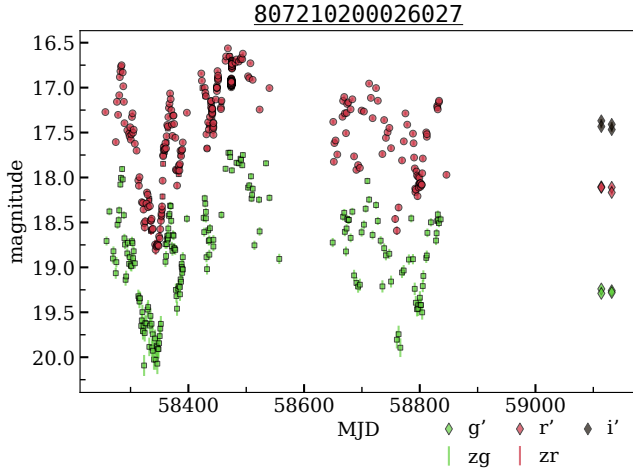


Figure 8. The light curves of poorly classified variable object — pre-main-sequence star or slow red irregular variable candidate from the Disk field. OIDs: 807110200025843, 807210200026027, 1840103100026721, 1840203100059097. Diamonds show the additional g' , r' , i' observations performed with RC600 telescope of CMO SAI MSU.

young stellar object (YSO; Marton et al. 2016). However, the light curve seems to be typical for slow red irregular variables, LB type, according to the General Catalogue of Variable Stars classification system (Fig. 8), which does not contradict the *Gaia* parallax.

4.3.2 Eclipsing binaries

Among the unclassified objects we identified six new eclipsing binaries (807203200013118, 807204200004799, 807204400014494, 807208400036953, 807211400009493, 807216400013229). As an example, Figure 9 shows the folded light curve of the object 807204200004799 in zr , zg passbands.

4.3.3 Unclassified Variables

Two other unclassified objects — 807212100012737, 807210200004045 — show non-periodic variability with an amplitude > 1 mag. Their light curves are shown in Figs. 10 and 11. We also obtained the observations with the RC600 telescope of CMO SAI MSU in g' , r' , i' passbands (Table 4). The variability is still present. Both objects do not have a significant IR excess. The distance to 807212100012737 is ~ 1000 pc. Based on this distance, brightness and colours we can make a dubious assumption that 807212100012737 is a red dwarf with strong spot activity. The distance to 807210200004045 is poorly defined; the *Gaia*

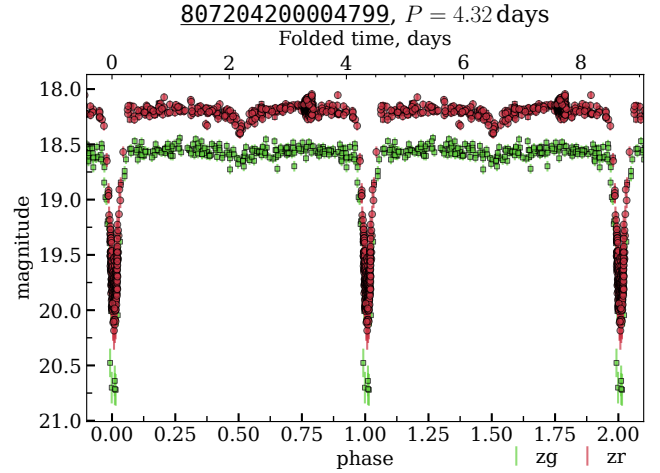


Figure 9. The folded light curves of 807204200004799 from the Disk field classified by us as an eclipsing binary. OIDs: 807104200003543, 807204200004799, 1809109100009148, 1809209100012225, 1810112100013288, 1810212100046961.

parallax to error ratio is 1.14. Therefore, we do not make any assumption about its nature.

4.4 Bogus

The ZTF data processing pipeline includes a procedure to separate the astrophysical events from bogus, i. e. false positive detections (Masci et al. 2019). However, among the outliers we encountered a significant fraction of bogus light curves (80/101, 95/113, 13/63 for the M 31, DEEP, DISK fields, respectively). A few examples are:

- (i) a point sharply dropping up or down by several magnitudes — possibly due to satellite/plane tracks, double star in one aperture due to defocusing, bad columns on CCDs, or cosmic particles;
- (ii) a random spread within several magnitudes due to ghosts, diffraction spikes, bright stars halos, cosmic rays or wrong background subtraction (close to M 31 centre);
- (iii) a combination of (i) and (ii).

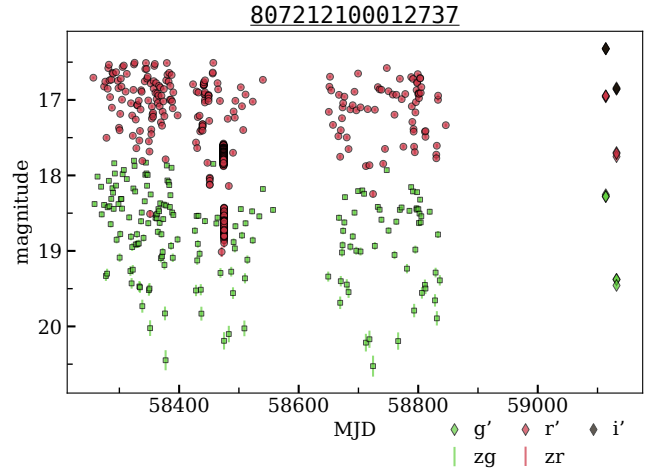
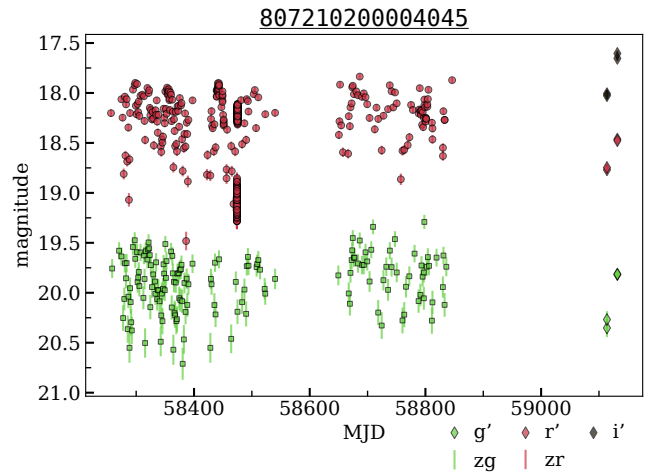
Bogus examples with suggested classification are given in Fig. 12. We discuss below some interesting cases.

4.4.1 795205400022890 and its echoes

In our outlier list there are four variables with the same phase and period. We found that one of them, known as IW Dra, is a typical Mira variable, while three others are located in $\sim 20''$ region around it. It turned out that these three neighbours are artefacts of

Table 3. Photometric observations of the candidates to pre-main-sequence sources with RC600 telescope of the Caucasus Mountain Observatory, SAI MSU.

MJD	Filter	Magnitude	Error
807206200003542			
59114.06219	<i>g'</i>	16.916	0.010
59114.06499	<i>g'</i>	16.930	0.010
59114.06780	<i>g'</i>	16.911	0.011
59132.84609	<i>g'</i>	16.046	0.006
59132.84720	<i>g'</i>	16.052	0.006
59114.06319	<i>r'</i>	15.592	0.006
59114.06600	<i>r'</i>	15.597	0.006
59114.06881	<i>r'</i>	15.588	0.006
59132.84437	<i>r'</i>	14.900	0.004
59132.84514	<i>r'</i>	14.901	0.004
59114.06403	<i>i'</i>	14.833	0.005
59114.06683	<i>i'</i>	14.823	0.005
59114.06964	<i>i'</i>	14.830	0.005
59132.84283	<i>i'</i>	14.249	0.004
59132.84359	<i>i'</i>	14.252	0.004
807206200004116			
59114.07549	<i>g'</i>	20.150	0.180
59132.82983	<i>g'</i>	20.587	0.160
59132.83456	<i>g'</i>	20.480	0.096
59132.83812	<i>g'</i>	20.310	0.087
59114.07953	<i>r'</i>	18.534	0.047
59114.08100	<i>r'</i>	18.546	0.055
59132.82603	<i>r'</i>	18.949	0.059
59132.82783	<i>r'</i>	18.887	0.054
59114.08235	<i>i'</i>	17.587	0.047
59114.08347	<i>i'</i>	17.529	0.049
59132.82239	<i>i'</i>	18.369	0.106
59132.82420	<i>i'</i>	18.195	0.057
807206200014645			
59114.03133	<i>g'</i>	17.780	0.016
59114.03279	<i>g'</i>	17.782	0.016
59114.03426	<i>g'</i>	17.805	0.016
59132.81479	<i>g'</i>	18.379	0.058
59132.81625	<i>g'</i>	18.285	0.066
59132.81771	<i>g'</i>	18.358	0.075
59114.03544	<i>r'</i>	16.997	0.013
59114.03621	<i>r'</i>	17.031	0.014
59114.03699	<i>r'</i>	16.992	0.013
59132.81127	<i>r'</i>	17.535	0.034
59132.81238	<i>r'</i>	17.532	0.034
59132.81349	<i>r'</i>	17.506	0.040
59114.03781	<i>i'</i>	16.386	0.013
59114.03859	<i>i'</i>	16.391	0.013
59114.03936	<i>i'</i>	16.384	0.012
59132.80879	<i>i'</i>	16.832	0.034
59132.80955	<i>i'</i>	16.829	0.037
59132.81031	<i>i'</i>	16.905	0.038
807210200026027			
59113.8449916	<i>g'</i>	19.240	0.033
59113.8485605	<i>g'</i>	19.290	0.034
59131.8365898	<i>g'</i>	19.259	0.039
59131.8401575	<i>g'</i>	19.280	0.039
59113.8513134	<i>r'</i>	18.103	0.022
59113.8531301	<i>r'</i>	18.111	0.022
59131.8430829	<i>r'</i>	18.109	0.023
59131.8452469	<i>r'</i>	18.167	0.024
59113.8549981	<i>i'</i>	17.369	0.019
59113.8568122	<i>i'</i>	17.433	0.020
59131.8472884	<i>i'</i>	17.467	0.024
59131.8491064	<i>i'</i>	17.409	0.025

**Figure 10.** The light curves of unclassified variable object from the Disk field. OIDs: 807112100008284, 807212100012737. Diamonds show the additional *g'*, *r'*, *i'* observations performed with RC600 telescope of CMO SAI MSU.**Figure 11.** The light curves of unclassified variable object from the Disk field. OIDs: 807110200019782, 807210200004045. Diamonds show the additional *g'*, *r'*, *i'* observations performed with RC600 telescope of CMO SAI MSU.

the automatic ZTF photometry arising from incorrect background subtraction of the halo of a bright variable star which overlaps with the light from the nearby objects. The light curves of IW Dra and its echoes are shown in Fig. 13.

4.4.2 807203300039547 — overlap of star and known asteroid

One short transient was identified as a conjunction of asteroid 945 (Barcelona) and a weak star in the Disk field (Fig. 14). The identification of the asteroid was performed with SkyBot (Berthier et al. 2006).

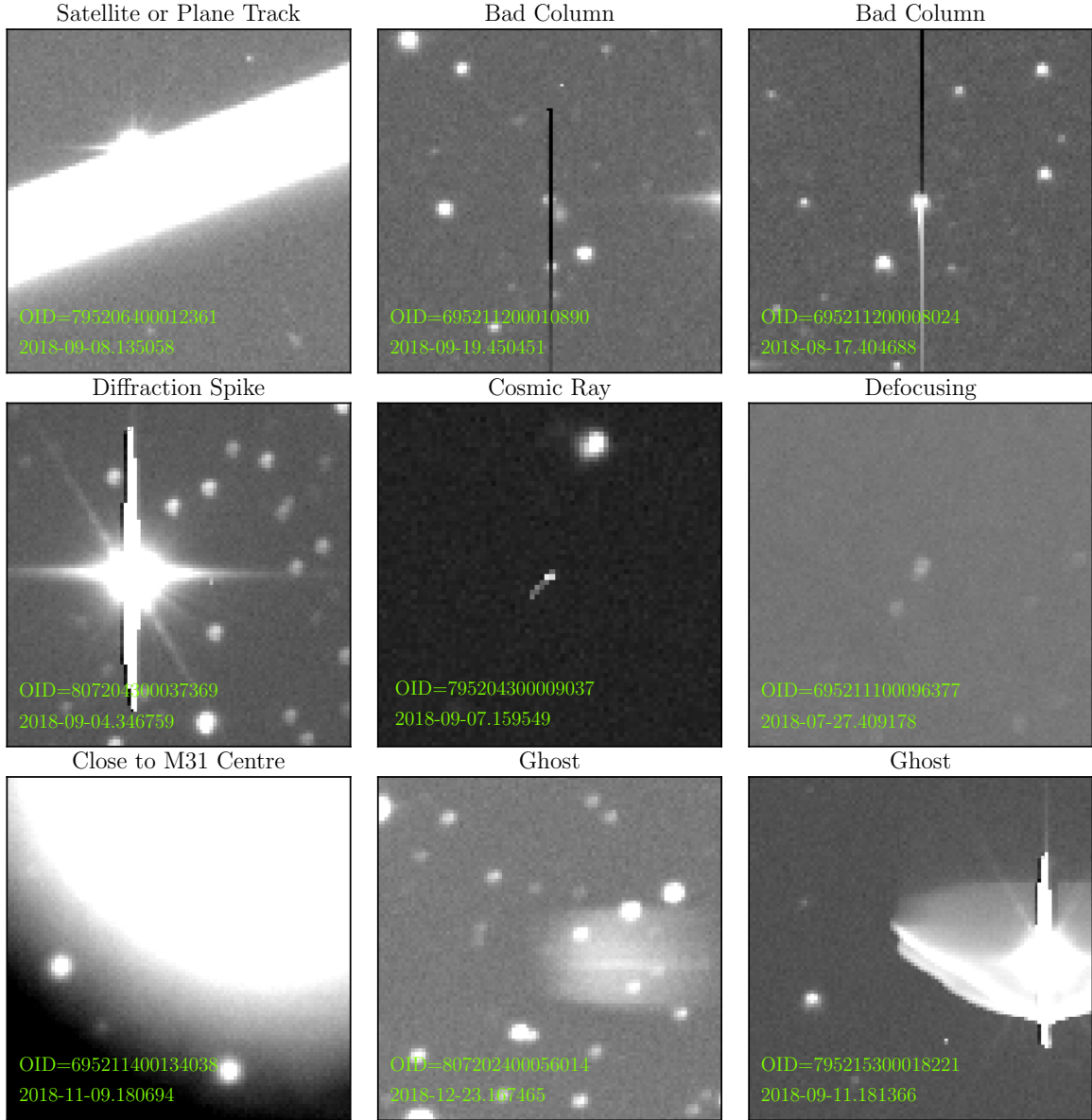


Figure 12. Cases of bogus detections found among the outliers. The outlier is located in the image centre. The size of the cutout showing a cosmic ray is 70×70 CCD pixels, for the others the image size is 100×100 CCD pixels.

4.4.3 695211200077906 — double star artefact

We found several objects that show bogus variability, and identified them as double stars with $\sim 2''$ separation. We assume that bogus measurements occur due defocusing when the FWHM becomes significantly larger than the separation between the components of the double star, which leads to overstatement of the object brightness. The example of such a bogus light curve is 695211200077906, see Fig. 15, where positions are given by the ZTF Lightcurve API¹¹.

¹¹ In this particular case we used the API because the individual observations coordinates are missed in the bulk-downloadable files. API description page is https://irsa.ipac.caltech.edu/docs/program_interface/ztf_lightcurve_api.html

5 PIPELINE VALIDATION

In order to access the efficiency of our pipeline in identifying light curves with significantly different properties than those already present in the bulk of ZTF DR3 data, we created validation test-sets adding a few artificially generated light curves to the real data. This set of enclosed light curves is inspired by potentially interesting astrophysical sources, as well as example cases of non-existing objects. The last case includes a perfectly plateau “Flat Without Noise” light curve, “Flat With Noise” which represents non-variable source, “Point Up”, “Point Down”, “Step Up”, and “Step Down” mimicking a rapid magnitude change or bad column. The astrophysically motivated fakes were built from 1) confirmed binary microlensing events Gaia16aye (three different parts of its r light

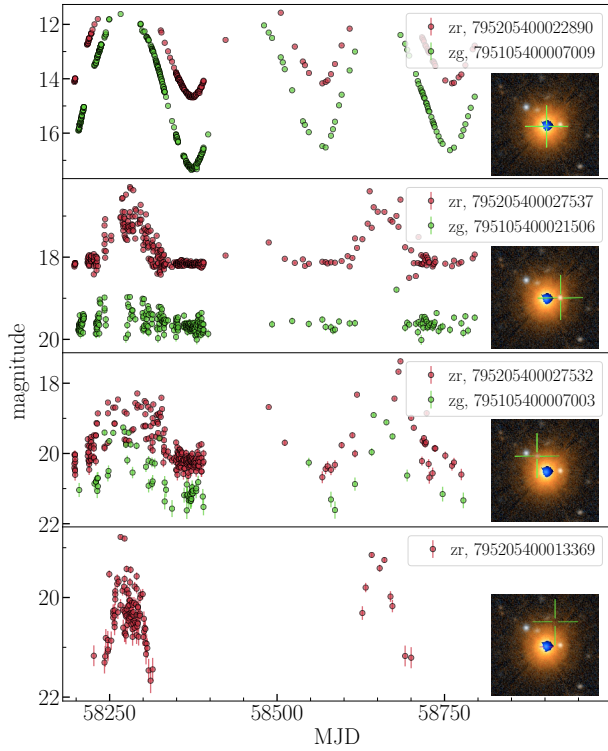


Figure 13. IW Dra and its echoes. SDSS image shows the position of IW Dra and three ZTF sources showing the correlated variability.

Figure 14. Asteroid Barcelona overlapping object 807203300039547. The blue crosses mark the location of the ZTF transient detection. An animated version is available in the electronic version.

Table 4. Photometric observations of unclassified variable objects with RC600 telescope of the Caucasus Mountain Observatory, SAI MSU.

MJD	Filter	Magnitude	Error
807210200004045			
59113.82463	g'	20.352	0.091
59113.82820	g'	20.268	0.084
59131.79666	g'	19.818	0.048
59131.80022	g'	19.813	0.049
59113.83096	r'	18.769	0.039
59113.83277	r'	18.746	0.038
59131.80315	r'	18.462	0.027
59131.80531	r'	18.478	0.028
59113.83464	i'	18.007	0.034
59113.83645	i'	18.027	0.035
59131.80736	i'	17.654	0.027
59131.80917	i'	17.605	0.026
807212100012737			
59113.79655	g'	18.256	0.026
59113.79802	g'	18.278	0.026
59113.79948	g'	18.281	0.026
59131.77430	g'	19.380	0.058
59131.77697	g'	19.376	0.043
59131.77937	g'	19.457	0.045
59113.80083	r'	16.960	0.012
59113.80194	r'	16.948	0.012
59113.80305	r'	16.946	0.012
59131.78118	r'	17.697	0.020
59131.78230	r'	17.751	0.022
59131.78342	r'	17.711	0.021
59113.80422	i'	16.325	0.011
59113.80533	i'	16.321	0.011
59113.80644	i'	16.320	0.011
59131.78459	i'	16.857	0.017
59131.78571	i'	16.856	0.017
59131.78683	i'	16.841	0.016

curve, Wyrzykowski et al. 2016), and candidates ZTF18ablruzq and ZTF18acskgwu (zr passband, Mróz et al. 2020), 2) single microlensing events ZTF18aaztjyd and ZTF18abaqxrt (zr passband, Mróz et al. 2020), 3) r light curve of kilonova 170817 (Villar et al. 2017), 4) V light curve of cepheid in eclipsing binary OGLE-LMC-CEP-0227 (Soszynski et al. 2008).

Original light curves were modified to conform with ZTF DR3 cadence and noise levels. We used a cubic smoothing spline fit for approximation of real objects and sampled the resulting function according to the cadence of real ZTF DR3 objects: 695211200035023 (for M31 field), 795216100016711 (for DEEP field) and 807201300060502 (for DISK field). The uncertainty of each observation was assigned using a linear relation between observed magnitude and its error, but with a lower bound of 0.001 mag. To derive this linear relation we took all zr observations in the DISK field with `catflag = 0`, averaged their magnitudes and uncertainties in intervals of 0.01 mag, and fitted these binned uncertainties with a linear function of magnitude, resulting in:

$$\delta = \max(0.001; 0.0297 m - 0.4179).$$

Fit parameters for the other fields agree with this relation within 20% margin. The final light curves for all fakes are shown in Fig. 16.

We built three validation data sets adding fifteen fake anomalous light curves to each of them and applied the same outlier detection algorithms as used for the ZTF data. The resulting detection rates are shown in Fig. 17, where “union” denotes the total rate of all used algorithms run in parallel. M31 field is the smallest one, so the percent of outliers the expert can examine is the largest. This

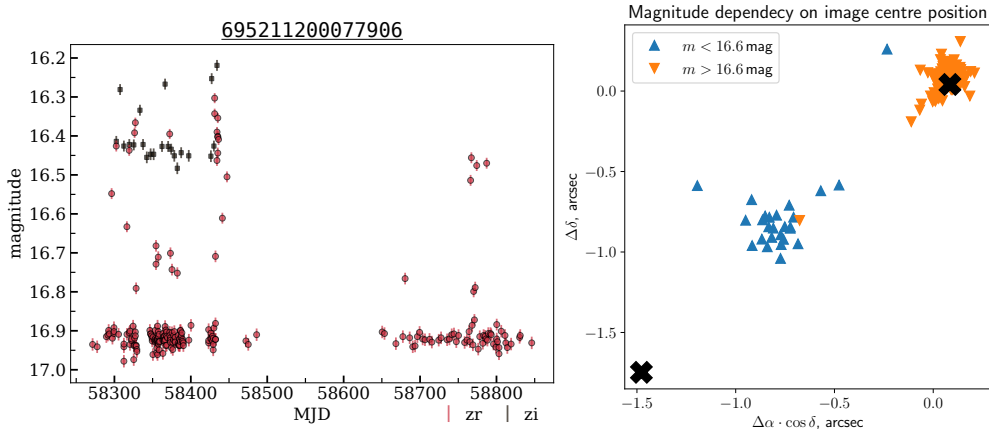


Figure 15. The light curves and the image centre positions of 695211200077906. **Left:** light curves, OIDs: 695211200077906 (zr , red circles), 695311200089204 (zi , black squares). **Right:** spatial distribution of observations relative to the average object position, black crosses show Gaia DR2 positions of the double star components. Note that the small brightness ($m > 16.6$ mag) of the object corresponds to the position of one of the components, while the large brightness ($m < 16.6$ mag) corresponds to the position somewhere between the components. We assume that the reason of such correlation between magnitude and position is in different FWHM of point spread function in different observations: for the first case FWHM is $\sim 2''$ and photometry counts signal from one component only, but for the other case FWHM is $\sim 4''$ and both components are being described by the common integrating area which makes measured magnitude closer to the integral magnitude of the double star and position to be near the double star centre.

is why the very first 32 outliers contain 13 of 15 fake anomalies, while OGLE-LMC-CEP-0227 is the 408th and “Flat With Noise” the 3630th outlier. We use only three algorithms (IF, GMM & O-SVM) for DEEP field, but the fake detection rate is still very high, probably because its light curves are less diverse and the fake anomalies are more different. The first 30 outliers contain 11 fakes, while ZTF18ablruzq and ZTF18acskgwu are found within the first 700 outliers, OGLE-LMC-CEP-0227 and “Flat With Noise” are within the first 6000 objects. The Disk field contains ~ 1.8 million objects and we used IF & GMM only, but the fake performance is quite acceptable: first 8 fakes are found within the first 90 outliers, 14 of 15 fakes are found within the first 1200 outliers, and only “Flat With Noise” was not detected until the 400 000th outlier. These results show that the outlier detection pipeline shows good anomaly detection rate and could detect physically interesting events. The “Flat With Noise” object is the hardest fake light curve to detect by all algorithms in all fields. This is possibly due to its location in a dense region of feature space which is also populated with low-variable sources and variable sources below ZTF’s threshold of detectability, or even stochastic variance stemming from a small subset of objects marked as variable from within a large distribution of non-variable objects.

6 EXPLORATORY DATA ANALYSIS

Once the experts finished their investigation we can now use the accumulated knowledge to identify simple strategies which would allow us to quickly separate interesting anomaly candidates from bogus light curves. We start with an exploratory data analysis (EDA) of our feature space. Figure A1 shows histograms for all features and fields. In what follows we give an example EDA performed over the incremented parameter space, which includes features as well as the expert judgement.

Figure A2 shows the separate feature distribution for bogus objects and anomaly candidates in the M31 field. From this, it is evident that Periodogram Amplitude and Reduced χ^2 possess complementary dissimilar distributions between the two classes.

Analysing the relationship between these two features (Fig. 18) we see that it is possible to identify bogus light curves as those presenting low Periodogram Amplitude (frequently caused by chaotic signals) and high Reduced χ^2 values (when one or more images of some real source is overlapping with another source, such as a bad column or a glare, which mimics a constant light curve with bright outbursts).

We emphasise that the expert-tagging of objects was performed prior to the EDA, and the overall near-orthogonal distribution of objects in the M31 field did not influence the expert’s analysis.

Although we do not expect a 2-dimensional parameter space to completely enclose the complexity of a real/bogus separation pipeline, it is reasonable to assume that, for each data set, some low-dimensional representation will enable quick identification of these 2 classes — even if we do not expect the final classification to be perfect. This is a direct example of how we can harvest expert knowledge to optimise further automatic identifications. Similar approaches may be used to construct powerful alert stream filters in the context of real-time alert brokers like ANTARES (Narayan et al. 2018; Matheson et al. 2020), ALERCE (Förster et al. 2020), and Fink (Möller et al. 2020). Further exploration of feature phase-space anomaly detection is currently a main focus in Aleo *et al.* (in prep.).

6.1 Principal Components

Principal Component Analysis (PCA, Jolliffe 2013) is a dimensionality-reduction technique whereby multidimensional data are decomposed into an orthogonal basis following the directions of maximum data variance. We implemented the PCA module using the sklearn Python package (Pedregosa et al. 2011), and normalised the feature values across all objects using the StandardScaler module. Subsequently, we calculated 42 Principal Components (PCs), ordered by those which explain the most variance. For the M31 field, the first two PCs together explain 47.1% of the variance, with the first 15 explaining 90.4%. Likewise, for the DEEP and DISK fields the first two PCs together explain 49.7%, and 50.2% of the variance, respectively.

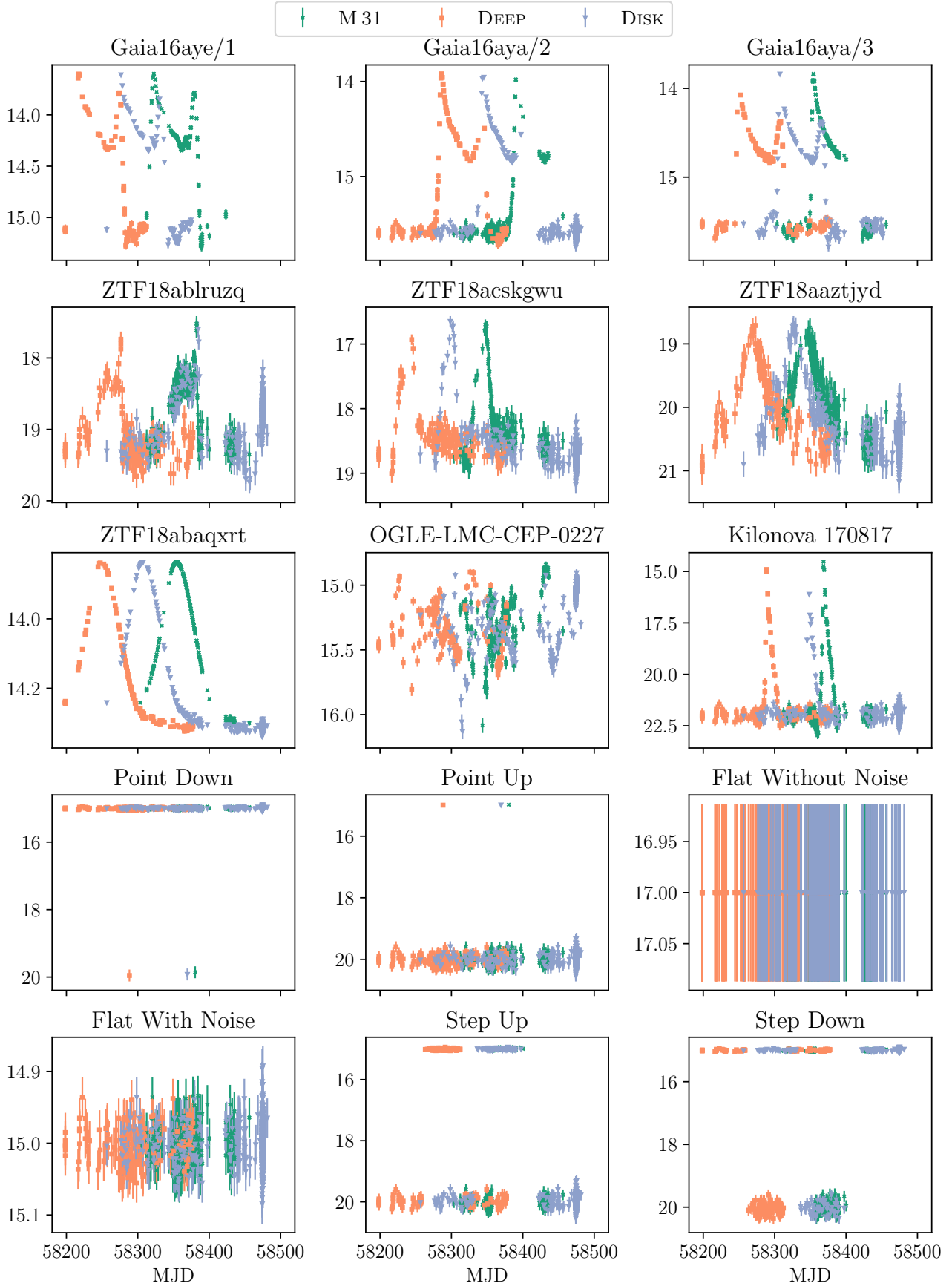


Figure 16. Fake z_r light curves. Time-shift between different fields is caused by different initial observational date for each field. We show the light curves following cadences of M 31 (green), DEEP (orange) and DISK (blue) fields.

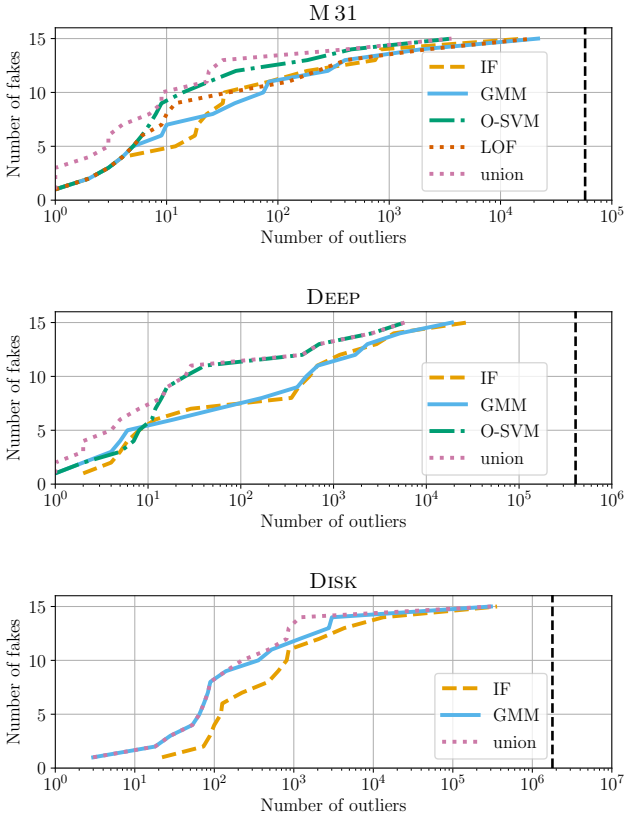


Figure 17. Fake detection rate. “Union” shows the total performance of all algorithms being run in parallel. Vertical dashed line shows the total number of light curves.

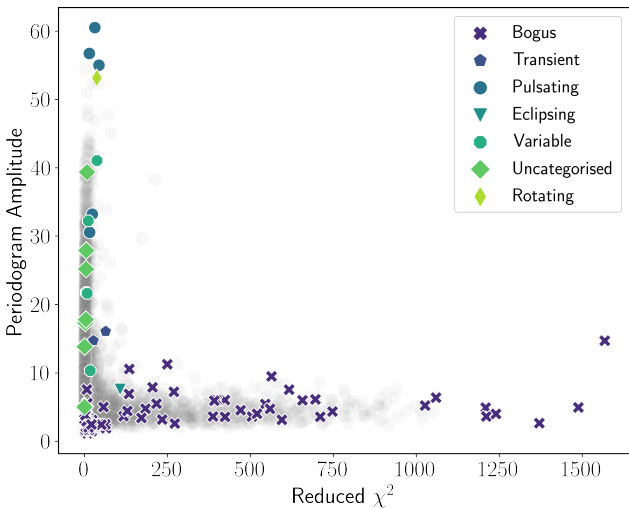


Figure 18. A scatter plot of the 101 M31 expert-tagged outliers in a Periodogram Amplitude—Reduced χ^2 phase-space. The bogus objects can be well separated from anomaly candidates. All 57 546 M31 objects are shown as grey circles.

The contribution to the first 2 PCs (loadings) from each of the 42 features are shown in Figure 19. For PC 1, shown in black, Standard Deviation, Inter Percentile Range 10%, and Percent Difference Magnitude Percentile 5% are the highest contributors. For PC 2, shown in magenta, Periodogram Amplitude, Periodogram Percent Amplitude, and Periodogram Beyond 2 Standard Deviations are those which contribute the most. From this, we note that PC 1 favours magnitude-based differences, and PC 2 favours periodogram-based features across all three fields. This is expected, since the two categories of information are complementary.

This complementarity is also evident in the correlation matrix of normalised feature values (Fig. A3). We see clearly two separate sets of features highly correlated between themselves and weakly correlated with members from the other group. This may be indicative that some features are degenerate. In fact, in Figure A1, those features with similar correlation vectors share similar distributions, albeit different values. However, since no singular feature had a consistently negligible contribution across all PCs and given the fluctuation in contribution by each features to successive PCs (19), we decided to keep all 42 features as input in our anomaly detection algorithm pipeline.

We show in Figure 20 distributions for the features with largest contribution to the first *three* PCs (PC 1—Standard Deviation, PC 2—Periodogram Amplitude, PC 3—Reduced χ^2) across all fields considering only objects identified as uncategorised anomaly candidates. All uncategorised anomaly candidates across the three fields are contained within, but do not constitute the edges of, their parent field distribution. That is, they are not in the tail of the distribution where the feature value is greatest, and are sometimes dwarfed in number by other objects in their field which make up their parent distribution. This could explain why such anomaly candidates were not yet categorised. These interesting, uncategorised candidates are high priority targets for future follow-up. See Section 4 and Table D1 for their listings.

7 CONCLUSIONS

Despite all the expected scientific results which inspired the construction of modern astronomical observatories, there is little doubt about the potential of the resulting data sets for new discoveries. In the era of systematic large scale sky surveys, a telescope which only fulfils its science goals cannot be considered successful (Norris 2017). In this context, the use of automatic machine learning tools is unavoidable. They provide important insights into the statistical properties and limits of the data set at hand, and can be optimised to be good recommendation systems. Nevertheless, the discovery itself will always be a profoundly human experience. In this context, the identification of scientifically interesting sources is a product of the combination of data-driven machine learning and human-acquired domain knowledge. The SNAD anomaly detection pipeline, presented in this work, and its accompany results, are a concrete example of how powerful such a system can be when applied to a rich data set as the ZTF DR3.

The pipeline consists of 3 separate stages: feature extraction, automatic outlier detection based on machine learning and anomaly confirmation by human experts. The infrastructure put in place to enable such detailed analysis includes not only the software pipeline¹² for feature extraction and outlier detection, but also a web-viewer¹³

¹² <https://github.com/snad-space/zwad>

¹³ <https://ztf.snad.space/>

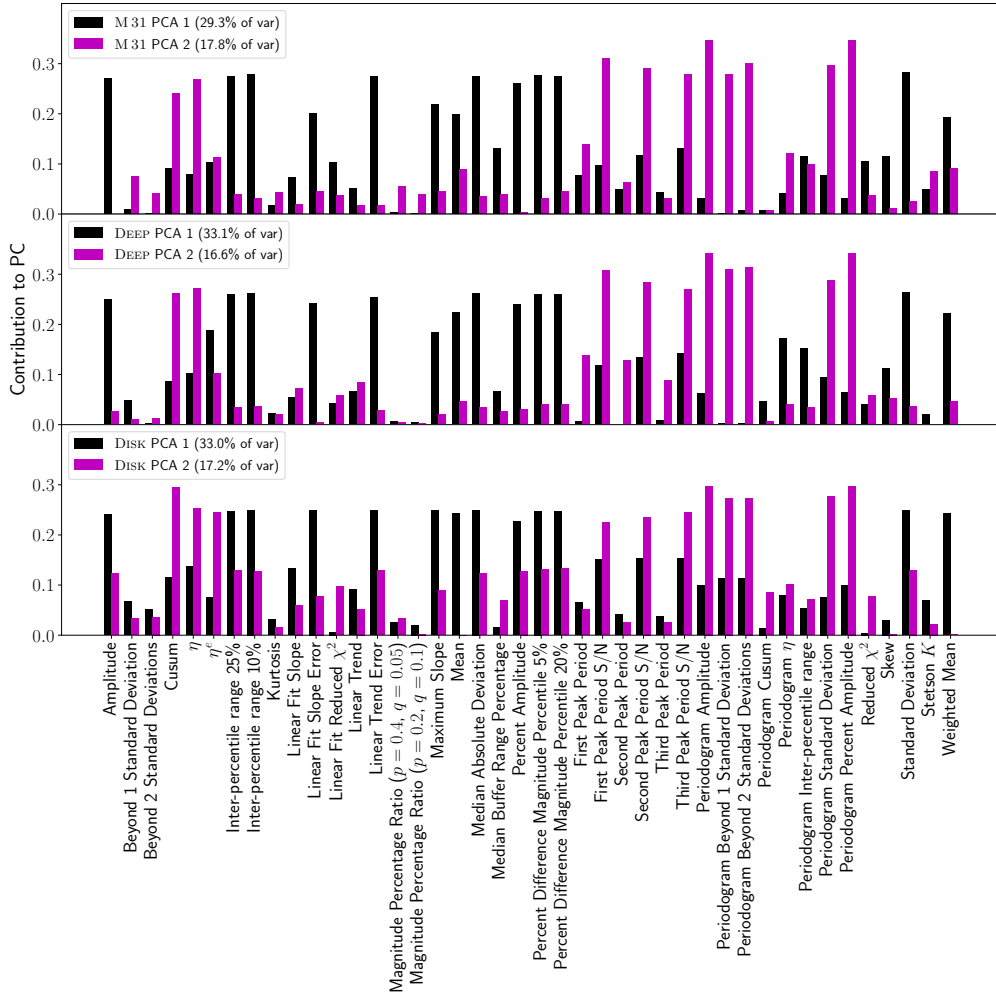


Figure 19. The first two principal components with ascribed feature loadings plotted for the M31 field (top panel, 47.1% of variance), DEEP field (middle panel, 49.7% of variance), and DISK field (bottom panel, 50.2% of variance). Notice that one principal component favours magnitude-based features (black), and the other favours periodogram and temporally-based features (magenta).

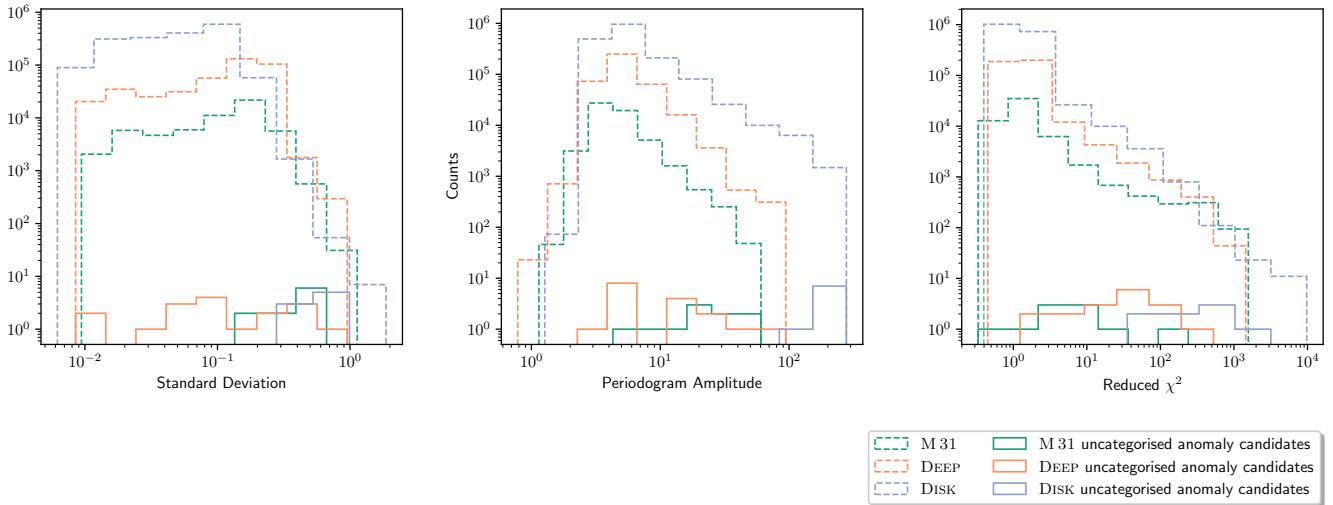


Figure 20. Distribution of features with largest contribution to the first 3 PCs for objects in M31 (dashed green), DEEP (dashed orange), and DISK (dashed blue) fields, as well as expert-identified uncatagorised anomaly candidates (solid contours).

allowing cross-match with multiple catalogues and external data source — specifically designed to help the expert in forming a global view of specific candidates. We apply the complete anomaly detection pipeline to three ZTF fields, corresponding to more than 2.25 million objects. Four outlier detection algorithms (Isolation Forest, Gaussian Mixture Model, One-Class Support Vector Machine and Local Outlier Factor) were used to identify the top 277 outliers. From these, the expert analysis concluded that 188 (68%) were bogus light curves and 89 (32%) real astrophysical sources – 66 of them being previously reported sources and 23 corresponding to non-catalogued objects.

For a few of the most interesting anomaly candidates, the expert analysis included gathering additional observational data. This allowed us to spectroscopically classify one anomaly candidate as a RS Canum Venaticorum star — a close detached binary whose variability outside the eclipse is due to stellar spots. Such objects are rare in ZTF DR3, therefore, we consider it an anomaly. Other found anomalies that belong to the rare types of objects are polar, supernovae and red dwarf flare. The interesting anomalies we found also include a few unclassified variable stars with controversial reports in the literature, among them the objects for which we performed the photometric observations. Nevertheless, additional studies are still required. We also found the sources that behave unusually for their suspected astrophysical type, e. g. the burst frequency of AT 2017ixs — possible nova in M31. Even among the bogus light curves we were able to identify interesting events, like the IW Dra star and its three companion echoes or the interaction of an asteroid with a background star.

Given the high incidence of bogus light curves, we searched for a simple rule which could allow us to easily estimate the likelihood of a given object being bogus. A quick exploratory data analysis, over the data accumulated by the expert, showed that bogus light curves are more likely to have a high reduced χ^2 and low period amplitude (at least for data in the M31 field). At this point, this result should be seen only as an indication that a careful exploitation of the parameter space by the expert can potentially lead to useful relations. If confirmed, such a relation could be used in the construction of alert stream filters for future telescopes.

Despite the encouraging results reported in this work, the incidence of bogus among the automatic identified outliers is still relatively high (68%). In order to use similar techniques in the context of future surveys like the Vera Rubin Observatory Legacy Survey of Space and Time or the Nancy G. Roman Space Telescope¹⁴, it is necessary to reinforce and optimise the interaction between the domain expert and the machine learning algorithm. We are currently working on adaptive strategies which are proven to perform well in such scenarios (Ishida et al. 2019) and intend to add similar capabilities to the SNAD pipeline. Nevertheless, this experiment confirms the potential of machine learning techniques in pointing non-standard elements within a large data set. The list of anomaly candidates provided here may be of use for scientists working in a broad range of domains and consists of a concrete example of the crucial role to be played by automatic pipelines in the future of astronomical discovery.

ACKNOWLEDGEMENTS

We are grateful to L. N. Berdnikov and S. V. Antipin for the helpful discussion on the physical nature of anomaly candidates.

M.V.K., V.S.K., K.L.M., A.A.V. and M.V.P. are supported by RFBR grant according to the research project 20-02-00779 for preparing ZTF data, implementation of the anomaly detection algorithm, and analysis of outliers. We used the equipment funded by the Lomonosov Moscow State University Program of Development. The authors acknowledge the support by the Interdisciplinary Scientific and Educational School of Moscow University “Fundamental and Applied Space Research”. P.D.A. is supported by the Center for Astrophysical Surveys (CAPS) at the National Center for Supercomputing Applications (NCSA) as an Illinois Survey Science Graduate Fellow. V.V.K. is supported by the Ministry of science and higher education of Russian Federation, topic № FEUZ-2020-0038. E. E. O. Ishida and S. Sreejith acknowledge support from CNRS 2017 MOMENTUM grant under project *Active Learning for Large Scale Sky Surveys*. Observations with TDS and data reduction (S.G.Z., A.V.D.) are supported by the Ministry of science and higher education of Russian Federation under the contract 075-15-2020-778 in the framework of the Large scientific projects program within the national project “Science”.

This research has made use of the International Variable Star Index (VSX) database, operated at AAVSO, Cambridge, Massachusetts, USA. This research has made use of data and/or software provided by the High Energy Astrophysics Science Archive Research Center (HEASARC), which is a service of the Astrophysics Science Division at NASA/GSFC. This research has made use of “Aladin sky atlas” developed at CDS, Strasbourg Observatory, France. This research has made use of the SIMBAD database, operated at CDS, Strasbourg, France. We acknowledge the usage of the HyperLeda database¹⁵. This research has made use of NASA’s Astrophysics Data System Bibliographic Services and following Python software packages: NUMPY (van der Walt et al. 2011), MATPLOTLIB (Hunter 2007), SCIPY (Jones et al. 2001), PANDAS (pandas development team 2020; Wes McKinney 2010), SCIKIT-LEARN (Pedregosa et al. 2011), ASTROPY (Astropy Collaboration et al. 2013, 2018), and ASTROQUERY (Ginsburg et al. 2019).

DATA AVAILABILITY

The ZTF light-curve data underlying this article are available in NASA/IPAC Infrared Science Archive¹⁶. Light-curve feature set is available in Zenodo, at <https://doi.org/10.5281/zenodo.4318700>. Other data underlying this article are available in the source code GitHub repository at <https://github.com/snad-space/zwad>.

APPENDIX A: FEATURES

We extracted 42 features from every light curve. For this purpose the library on Rust programming language was developed¹⁷.

¹⁴ <https://www.stsci.edu/roman>

¹⁵ <http://leda.univ-lyon1.fr>

¹⁶ <https://irsa.ipac.caltech.edu/>

¹⁷ <https://docs.rs/light-curve-feature/0.1.18/>

A1 Auxiliary Definitions

A1.0.1 Light Curve We define light curve as a list of triples of magnitude m_i , its error δ_i and observation time t_i , where $i = 0..N-1$ and N is the number of observations.

A1.0.2 Mean We define mean of the sample $\{x_i\}$ as

$$\langle x \rangle \equiv \frac{1}{N} \sum_i x_i. \quad (\text{A1})$$

A1.0.3 Weighted Mean We define weighted mean of the sample $\{x_i\}$ with corresponding observation errors $\{\Delta_i\}$ as

$$\bar{x} \equiv \frac{\sum_i x_i / \Delta_i^2}{\sum_i 1 / \Delta_i^2}. \quad (\text{A2})$$

A1.0.4 Standard Deviation We define standard deviation of the sample $\{x_i\}$ as

$$\sigma_x \equiv \frac{\sum_i (x_i - \langle m \rangle)^2}{N - 1}. \quad (\text{A3})$$

A1.0.5 Indicator Function The indicator function of a set A $I_A(x)$ is a function that equals unity when $x \in A$ and equals zero when $x \notin A$. For instance, $I_{x>0}$ equals unity for positive numbers and zero for non-positive.

A1.0.6 Distribution Quantile We define $Q_x(p)$ to be the R-5¹⁸ p th quantile (100 · p percentile) of $\{x_i\}$.

A1.0.7 Median We define $\text{Median}(x) \equiv Q_x(0.5)$.

A1.0.8 Periodogram We use Lomb–Scargle (Lomb 1976; Scargle 1982) periodogram as an estimation of spectral power of the light curve. Our periodogram implementation is based on "fast" algorithm (Press et al. 1992), an estimation of Lomb–Scargle periodogram which can be evaluated in $O(N_\omega \log N_\omega)$, where N_ω is a number of considered angular frequencies. This method requires interpolation of light curve to an evenly separated time grid, we used linear interpolation for this purpose (MACC = 1 in spread function, Press et al. 1992). We found periodogram values $P_k = P(\omega_k)$ on an evenly angular frequency grid $\{\omega_k\}$:

$$\begin{aligned} \omega_k &= k \Delta \omega, \quad k = 1..N_\omega, \\ \Delta \omega &= \frac{2\pi(N-1)}{NR(t_{N-1} - t_0)}, \\ N_\omega &= 2^{\lceil \log_2 \frac{M\pi}{\delta t \Delta \omega} \rceil}, \end{aligned} \quad (\text{A4})$$

where $\lceil \cdot \rceil$ denotes the ceiling function, δt is a typical time interval between observations, in our case it equals $\text{Median}(\Delta t_i)$, median time interval between consequential observations $\Delta t_i \equiv t_{i+1} - t_i$. R and M are coefficients which expand the grid to lower and higher frequencies respectively. We used $R = 10$ and $M = 2$ in our analysis.

A2 Feature Description

We follow feature names from the original papers when possible.

¹⁸ See Type-5 at <https://stat.ethz.ch/R-manual/R-devel/library/stats/html/quantile.html>

A2.0.1 Amplitude The half amplitude of the light curve:

$$\frac{\max(m) - \min(m)}{2}. \quad (\text{A5})$$

A2.0.2 Beyond n Std D’Isanto et al. (2016) The fraction of observations beyond $\langle m \rangle \pm n \sigma_m$:

$$\frac{\sum_i I_{|m - \langle m \rangle| > n \sigma_m}(m_i)}{N}. \quad (\text{A6})$$

We use $n = 1$ and $n = 2$ in our analysis.

A2.0.3 Cusum Kim et al. (2014) The range of magnitude cumulative sums:

$$\max_j(S_j) - \min_j(S_j), \quad (\text{A7})$$

where

$$S_j \equiv \frac{1}{N \sigma_m} \sum_{i=0}^j (m_i - \langle m \rangle). \quad (\text{A8})$$

A2.0.4 Von Neumann η Kim et al. (2014)

$$\eta \equiv \frac{1}{(N-1) \sigma_m^2} \sum_{i=0}^{N-2} (m_{i+1} - m_i)^2. \quad (\text{A9})$$

A2.0.5 η^e Kim et al. (2014) Generalisation of η A2.0.4 for unevenly time series.

$$\eta^e \equiv (t_{N-1} - t_0)^2 \frac{\sum_{i=0}^{N-2} \left(\frac{m_{i+1} - m_i}{t_{i+1} - t_i} \right)^2}{(N-1) \sigma_m^2}. \quad (\text{A10})$$

Our version of this feature differs from Kim et al. (2014).

A2.0.6 Inter-percentile range

$$Q_m(1-p) - Q_m(p). \quad (\text{A11})$$

We use $p = 0.1$ and $p = 0.25$ in our analysis.

A2.0.7 Kurtosis The kurtosis of the magnitude distribution

$$G_2 \equiv \frac{N(N+1)}{(N-1)(N-2)(N-3)} \frac{\sum_i (m_i - \langle m \rangle)^4}{\sigma_m^4} - \frac{3(N+1)^2}{(N-2)(N-3)}. \quad (\text{A12})$$

A2.0.8 Linear Trend The slope of the light curve and its standard deviation. Least squares fit of the linear stochastic model with unknown constant Gaussian noise magnitude Σ assuming observation errors to be zero:

$$m_i = c + \text{slope } t_i + \Sigma \varepsilon_i, \quad (\text{A13})$$

where c and Σ are constants, $\{\varepsilon_i\}$ are standard distributed random variables.

A2.0.9 Linear Fit The slope, its standard deviation and the reduced χ^2 of the light curve linear fit. Least squares fit of the linear stochastic model with Gaussian noise described by observation errors $\{\delta_i\}$:

$$m_i = c + \text{slope } t_i + \delta_i \varepsilon_i, \quad (\text{A14})$$

where c is a constant and $\{\varepsilon_i\}$ are standard distributed random variables.

A2.0.10 Magnitude Percentage Ratio D’Isanto et al. (2016) The ratio of p th and q th inter-percentile ranges (see A2.0.6):

$$\frac{Q_m(1-p) - Q_m(p)}{Q_m(1-q) - Q_m(q)}. \quad (\text{A15})$$

We used $p = 0.4$, $q = 0.05$ and $p = 0.2$, $q = 0.1$ in our analysis.

A2.0.11 Maximum Slope D’Isanto et al. (2016) Maximum slope between two sequential observations:

$$\max_{i=0..N-2} \left| \frac{m_{i+1} - m_i}{t_{i+1} - t_i} \right|. \quad (\text{A16})$$

A2.0.12 Mean See A1.0.2.

A2.0.13 Median Absolute Deviation D’Isanto et al. (2016) Median of the absolute value of the difference between magnitudes and their median:

$$\text{Median} (|m_i - \text{Median}(m)|). \quad (\text{A17})$$

A2.0.14 Median Buffer Range Percentage D’Isanto et al. (2016) Fraction of observations inside $\text{Median}(m) \pm n \times \text{Median}(m)$ interval:

$$\frac{\sum_i I_{|m - \text{Median}(m)| < n \text{Median}(m)}(m_i)}{N}. \quad (\text{A18})$$

We used $n = 0.05$ in our analysis.

A2.0.15 Percent Amplitude D’Isanto et al. (2016) Maximum deviation of magnitude from its median:

$$\max_i |m_i - \text{Median}(m)|. \quad (\text{A19})$$

A2.0.16 Percent Difference Magnitude Percentile D’Isanto et al. (2016) Ratio of p th inter-percentile range (see A2.0.6) to the median:

$$\frac{Q_m(1-p) - Q_m(p)}{\text{Median}(m)}. \quad (\text{A20})$$

We used $p = 0.05$ and $p = 0.2$ in our analysis.

A2.0.17 Periodogram Amplitude Same as Amplitude (see A2.0.1) but for $\{P_k\}$.

A2.0.18 Periodogram Beyond n Std Same as Beyond n Std (see A2.0.2) but for $\{P_k\}$. We used $n = 1$ and $n = 2$ in our analysis.

A2.0.19 Periodogram Cusum Same as Cusum (see A2.0.3) but for $\{P_k\}$.

A2.0.20 Periodogram η Same as Von Neumann η (see A2.0.4) but for $\{P_k\}$.

A2.0.21 Periodogram Inter-Percentile Range Same as Inter-Percentile range (see A2.0.6) but for $\{P_k\}$. We used $p = 0.25$ in our analysis.

A2.0.22 Periodogram Peaks Three highest periodogram peaks’ period and P_{peak}/σ_P (“signal-to-noise” ratio, Kim et al. (2014)), where σ_P is periodogram values standard deviation (see A2.0.23).

A2.0.23 Periodogram Standard Deviation Same as Standard Deviation (see A2.0.27) but for $\{P_k\}$.

A2.0.24 Peridogram Percent Amplitude Same as Percent Amplitude (see A2.0.3) but for $\{P_k\}$.

A2.0.25 Reduced χ^2 Reduced χ^2 of the plateau fit:

$$\frac{1}{N-1} \sum_i \left(\frac{m_i - \bar{m}}{\delta_i} \right)^2. \quad (\text{A21})$$

A2.0.26 Skew The skewness of magnitude distribution:

$$G_1 \equiv \frac{N}{(N-1)(N-2)} \frac{\sum_i (m_i - \bar{m})^3}{\sigma_m^3}. \quad (\text{A22})$$

A2.0.27 Standard Deviation σ_m , see A1.0.4.

A2.0.28 Stetson K Stetson (1996)

$$K \equiv \frac{\sum_i \left| \frac{m_i - \bar{m}}{\delta_i} \right|}{\sqrt{N \sum_i \left(\frac{m_i - \bar{m}}{\delta_i} \right)^2}}. \quad (\text{A23})$$

A2.0.29 Weighted mean \bar{m} , see A1.0.3.

APPENDIX B: ZTF DR OBJECTS WEB-VIEWER

We developed web-based graphical user interface for expert-analysis of outliers, however it can be used by any researcher working with ZTF DRs as a light-curve viewer and cross-match tool. We use ClickHouse¹⁹ column-based relation database management system as a storage for ZTF DR light-curves. A column-based database is sub-optimal for querying a small number of objects which is required by a web-service, but in our case the main purpose of the database was selecting of batches of objects for feature extraction for anomaly detection, while an opportunity of getting of individual objects is a useful by-product. The web-viewer is written on Dash²⁰ Python framework which is suitable for interactive data visualisation. An ZTF object page shows the main properties, light-curve and result of cross-matching with different catalogues. Due to the fact that several ZTF DR3 objects (OIDs) can represent the same source, the viewer shows not only light-curve of the current object, but also finds all neighbour ZTF DR light-curves within some radius, the default value is one arcsecond. A user can interact with the plot, changing this search radius, turn off and turn on light-curves, click on an observation to load image into embedded FITS viewer powered by JS9 library²¹. Also a user can see folded light-curve which can be useful for periodic variable star analysis. The object page contains cross-matching information with various variable star and transient catalogues, has embedded Aladin (Boch & Fernique 2014) Sky Atlas where object position is marked. Feature set which is presented in current paper (see Sec. A) is listed on the object page too. Web-viewer supports SIMBAD-powered (Wenger et al. 2000) object cone search which allows a user to find ZTF DR3 objects by common source name or by sky coordinates. A screenshot of the web-viewer is presented in Fig. B1 and its source code is available on Github²².

¹⁹ <https://clickhouse.tech>

²⁰ <https://dash.plotly.com>

²¹ <https://js9.si.edu>

²² <https://github.com/snad-space/ztf-viewer>

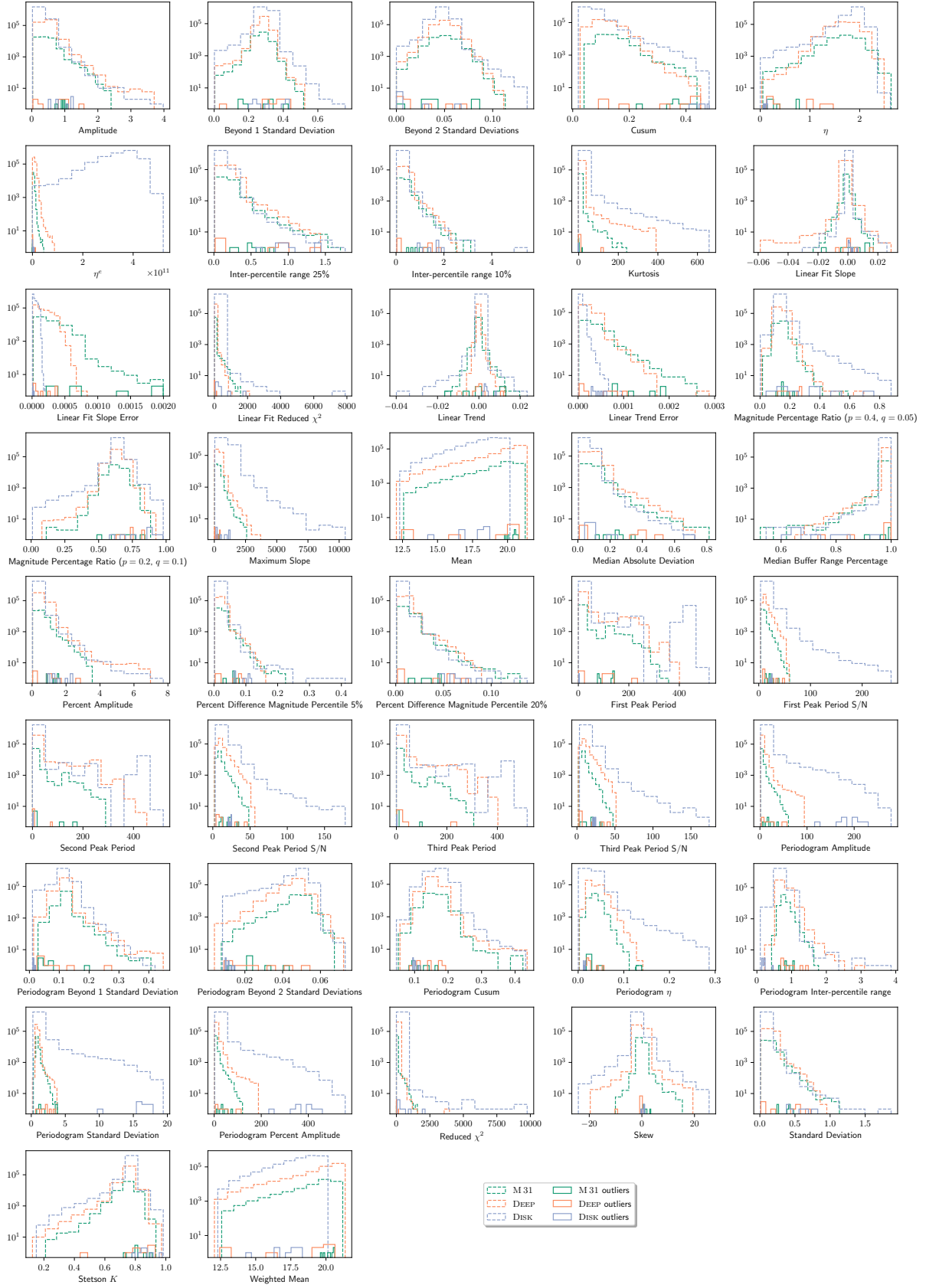


Figure A1. Histogram of all 42 light curve features for objects in M31 (dashed green), DEEP (dashed orange), and DISK (dashed blue), as well as outliers in M31 (solid green), DEEP (solid orange), and DISK (solid blue) fields.

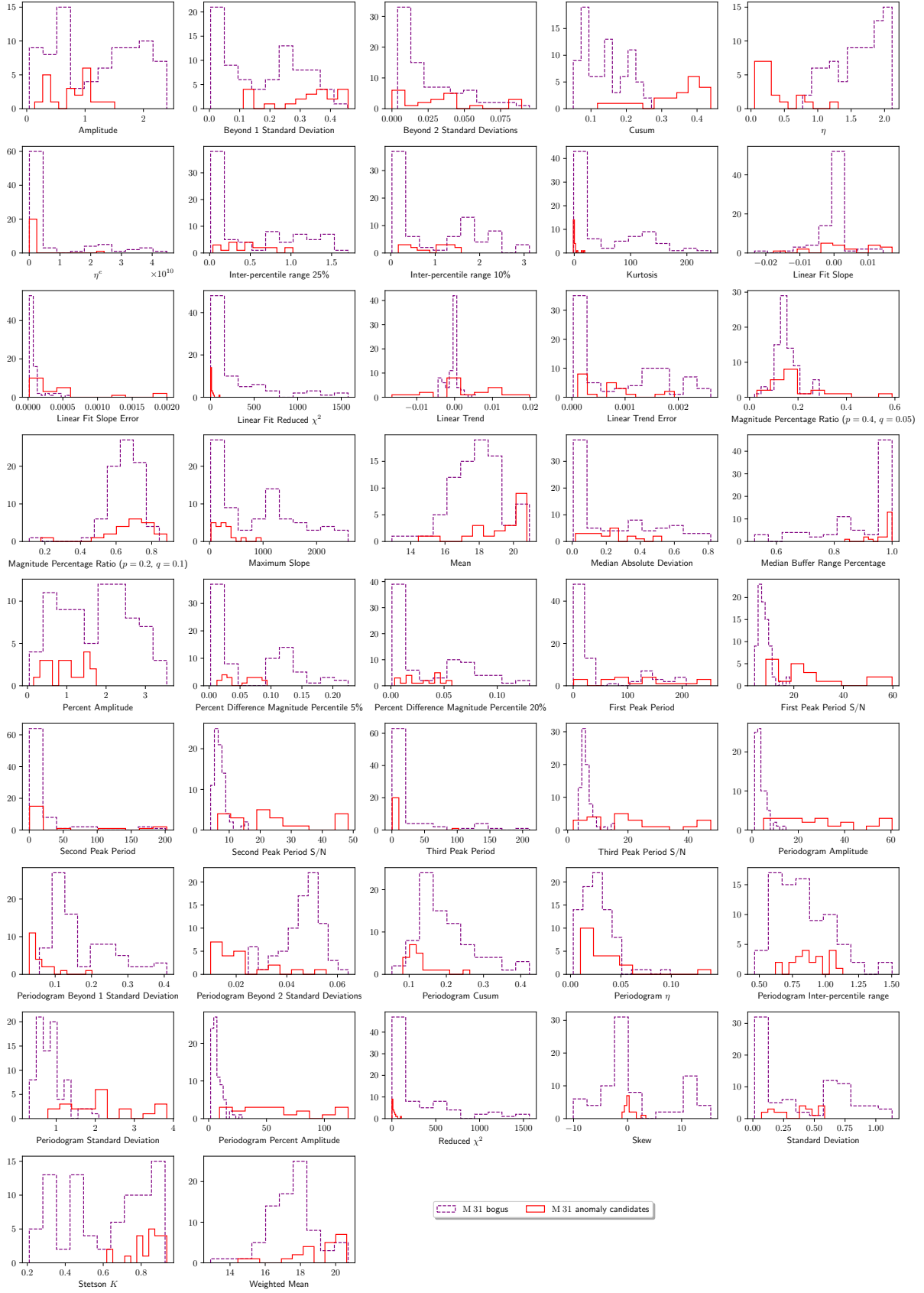


Figure A2. Histogram of all 42 light curve features in M 31 field for both bogus (dashed purple) and anomaly candidates (solid red).



Figure A3. A correlation matrix of all 42 light curve features on a combined data set of the M 31, DEEP, and DISK fields.

APPENDIX C: LIGHT CURVE FIT OF SUPERNOVA CANDIDATES

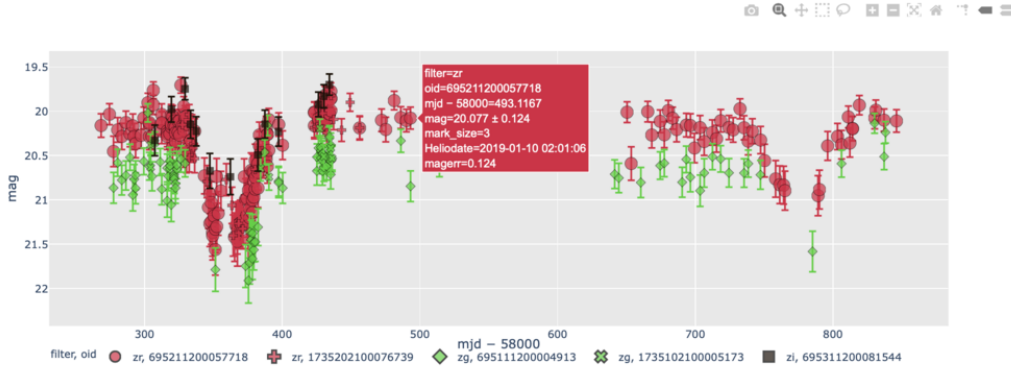
APPENDIX D: ANOMALY CANDIDATES

SNAD ZTF DR3 object viewer

OID
 Coordinates radius (arcsec)

695211200057718

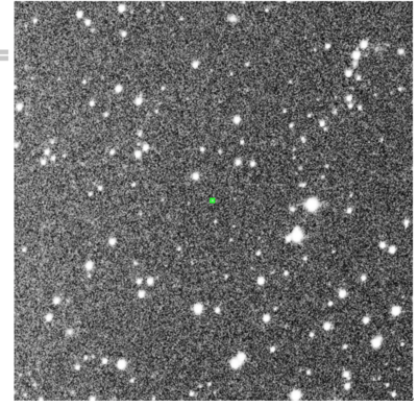
Short light curve: $58194.0 \leq \text{MJD} \leq 58483.0$
 Full light curve Folded light curve



Download [PNG](#), [PDF](#)

Summary

Name: [DBL2003] 12 (27.159" [Simbad](#))
Type: C* (27.159" [Simbad](#))
Period, days: 135.053 ([periodogram](#) S/N=16.690)



[Download FITS](#)

Aladin

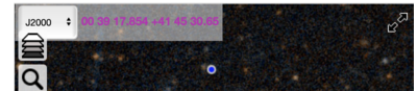


Figure B1. SNAD ZTF DR3 web-viewer page for object 695211200057718.

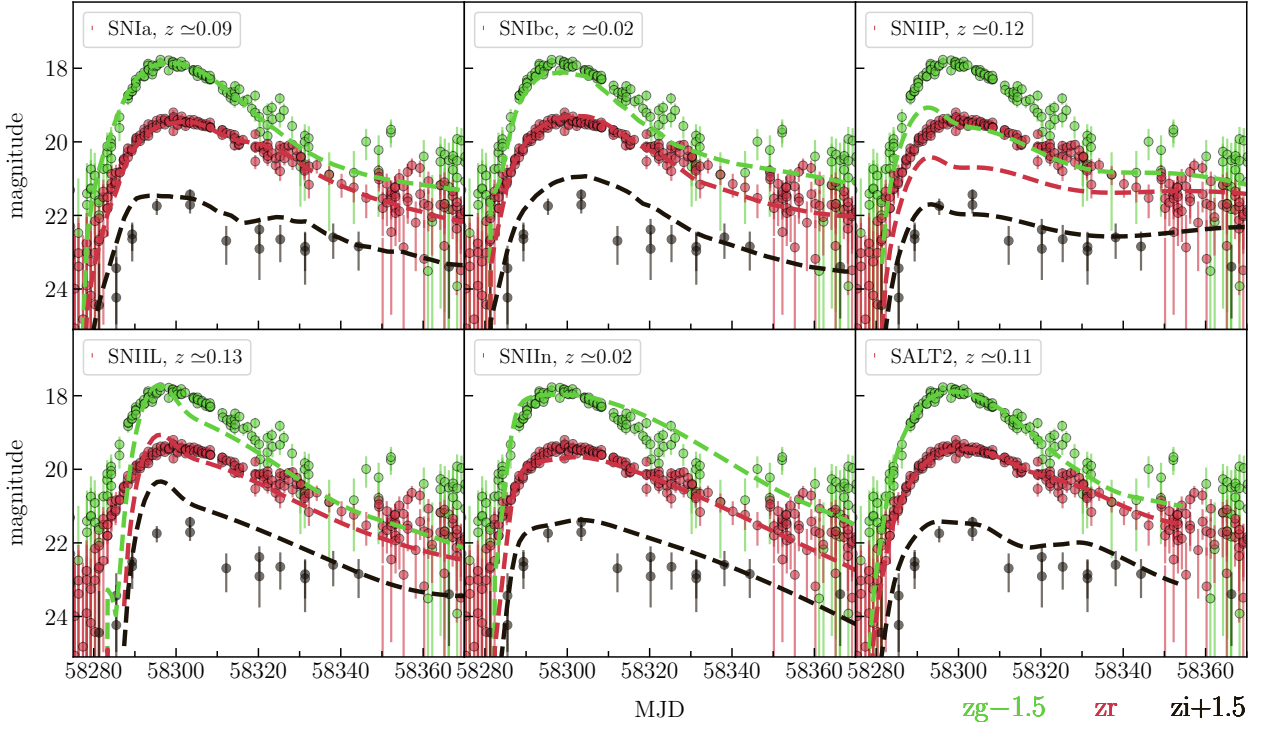


Figure C1. Results of light curve fit of 795209200003484 by Nugent's supernova models and SALT2 model. Observational data correspond to OIDs: 795109200001660 (z_g), 795209200003484 (z_r), 795309200004249 (z_i), 796312200003601 (z_i).

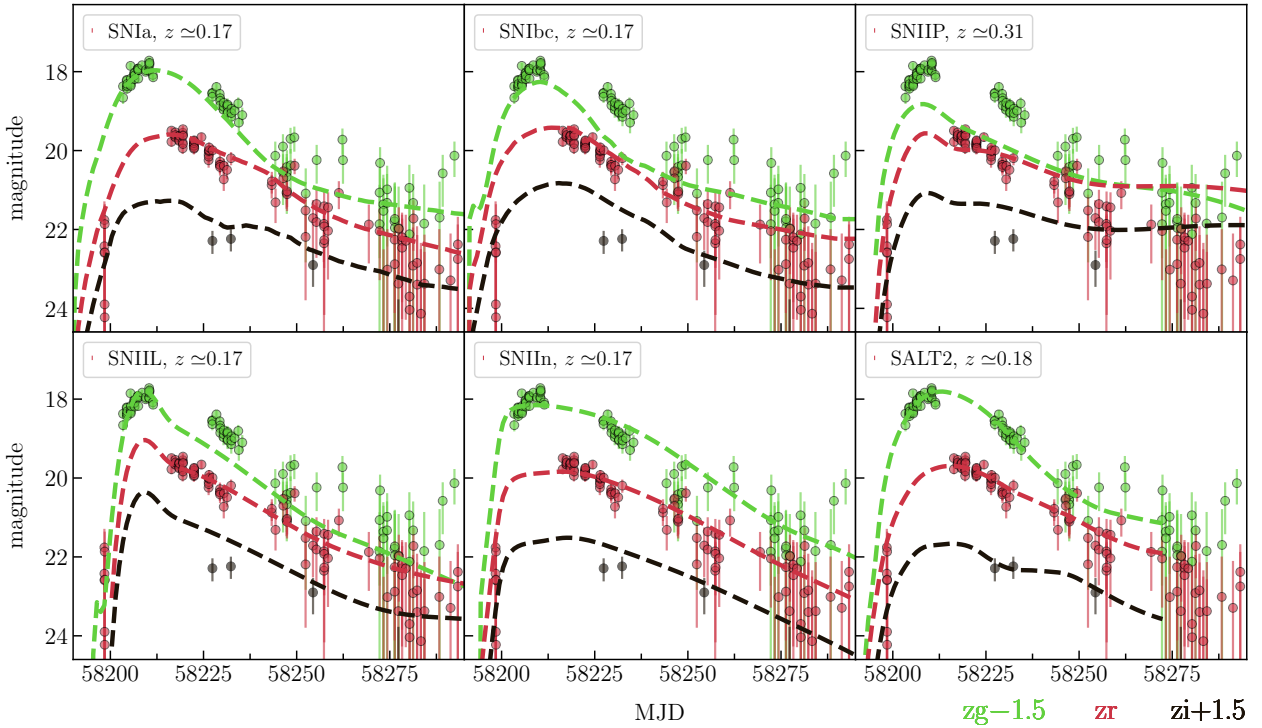


Figure C2. Results of light curve fit of 795212100007964 by Nugent's supernova models and SALT2 model. Observational data correspond to OIDs: 7951121000014865 (z_g), 795212100007964 (z_r), 795312100008834 (z_i).

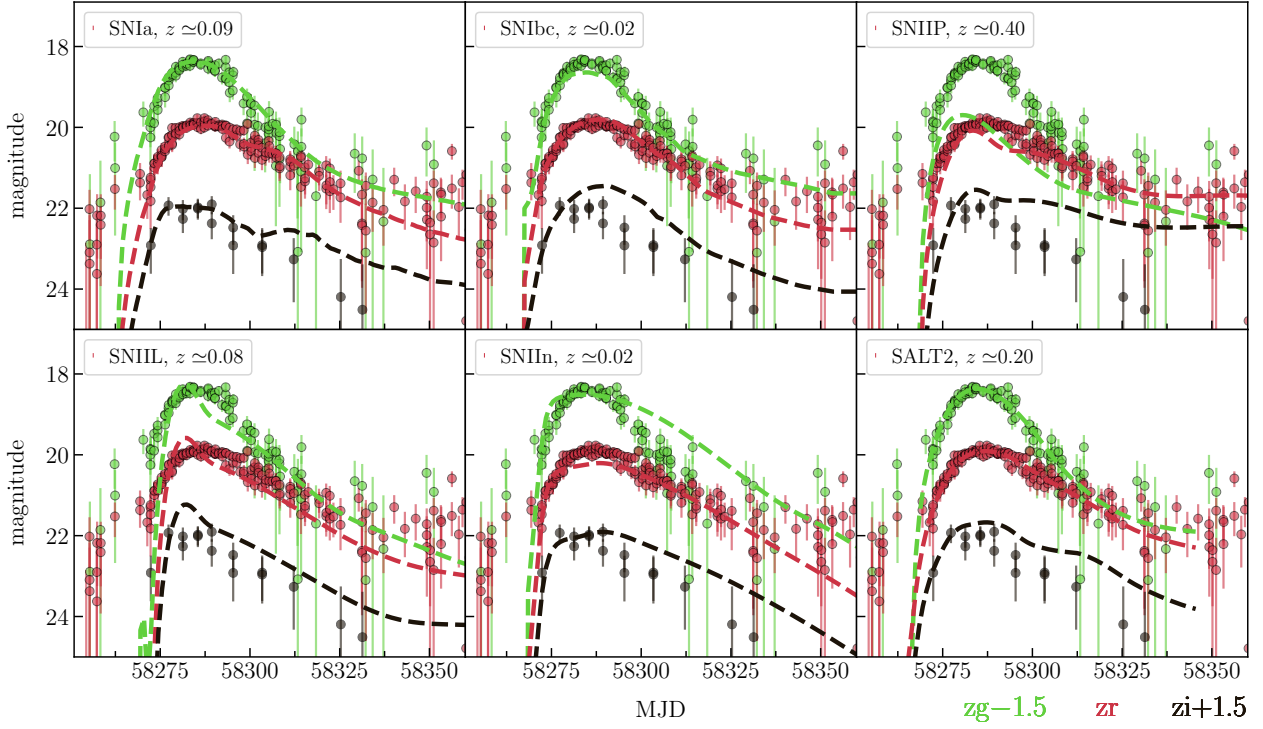


Figure C3. Results of light curve fit of 795205100007271 by Nugent's supernova models and SALT2 model. Observational data correspond to OIDs: 795105100002903 (z_g), 795205100007271 (z_r), 795305100008092 (z_i), 796308200008245 (z_i).

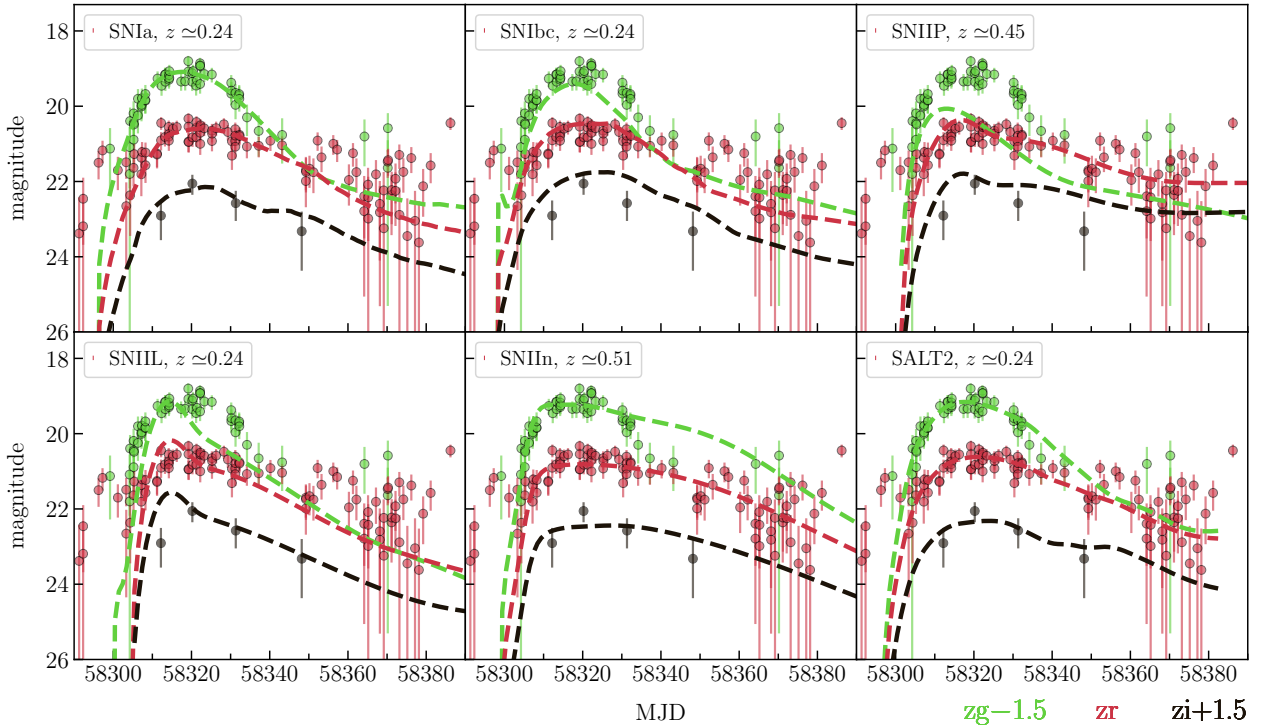


Figure C4. Results of light curve fit of 795204100013041 by Nugent's supernova models and SALT2 model. Observational data correspond to OIDs: 795104100011724 (z_g), 795204100013041 (z_r), 795304100015672 (z_i).

Table D1: A complete list of anomaly candidates in the M31, DEEP, and Disk fields.

OID	Other identifiers	α, δ (deg)	$m_{r,\min}$	$m_{r,\max}$	$E(B-V)$	D (pc)	$M_{r,\max}$	P_0^+ (d)	Type*	References
M31										
695211100003383	2MASS 100452494+4207269	11.35388 42.12427	20.87±0.25	18.71±0.05	0.117	M31	-6.05	—	RSG	[14]
695211100015190		11.79716 41.78059	21.45±0.31	19.49±0.09	0.078	M31	-5.17	—	—	
695211100022045	AT 2017ixs	10.98339 41.53641	21.27±0.29	18.66±0.05	0.268	M31	-6.50	—	PNV	[15]
6952111000131796	PSO J011.0457+41.5548	11.04581 41.55487	17.92±0.03	16.84±0.02	0.287	M31	-8.36	—	VAR	[16,17]
695211200018901	2MASS 100421755+4135039	10.57313 41.58447	18.54±0.04	17.78±0.02	0.143	M31	-7.06	214.6	RSG	[14]
695211200019653	2MASS 100415491+4133323, ZTFJ004154.90+413332.3	10.47879 41.55899	15.58±0.01	15.19±0.01	0.100	1642	3.85	7.715	MSINE, RSCVN	[2,3]
695211200022958	PSO J010.4744+41.4515	10.47441 41.45149	18.86±0.05	18.30±0.03	0.171	M31	-6.61	90.54	Delta Cep	[18]
695211200035023		10.50601 41.81453	21.17±0.25	19.33±0.07	0.061	M31	-5.29	132.9	—	
695211200046528	[MAP97] 55	10.63267 41.48622	18.51±0.04	17.85±0.02	0.308	M31	-7.41	74.29	Delta Cep	[19]
695211200057718		9.82489 41.76983	21.56±0.29	19.71±0.09	0.056	M31	-4.90	>200	—	
695211200058391		9.98496 41.74939	22.18±0.35	20.02±0.12	0.058	M31	-4.59	—	—	
695211200075348	M31N 2013-11b, MASTER OTJ004126.22+414350.0	10.35917 41.73029	21.61±0.29	19.40±0.07	0.060	M31	-5.22	168.4	VAR	[20,21]
695211300004359	PNV J00414894+4109173	10.45371 41.15395	20.61±0.21	17.56±0.03	0.261	M31	-7.58	—	PNV	[22]
695211300006331	CSS_J003827.1+410334	9.61336 41.05944	15.03±0.01	14.30±0.02	0.067	1546	3.18	3.138	EA	[1]
695211300007276	SV* SON 10726	10.19874 41.03242	18.51±0.05	17.78±0.03	0.275	M31	-7.40	58.00	Delta Cep	[23]
695211400009049		11.11946 40.99692	21.47±0.31	19.72±0.12	0.076	M31	-4.94	—	—	
695211400025927		11.44201 41.25969	21.82±0.34	20.07±0.16	0.072	M31	-4.58	—	—	
695211400027347	2MASS 100434749+4112585	10.94775 41.21573	21.50±0.31	19.57±0.11	0.332	M31	-5.76	>200	VAR	[24]
695211400046832		11.26142 40.57456	22.17±0.37	20.21±0.18	0.063	M31	-4.41	—	—	
695211400070144	2MASS 100443180+4119083	11.13252 41.31898	19.63±0.12	18.10±0.04	0.275	M31	-7.07	—	VAR	[25]
695211400121607	[JPN2003] V206	10.87915 41.09875	21.42±0.30	19.33±0.09	0.181	M31	-5.60	—	VAR	[24]
DEEP										
7952021000005941	MLS180307:163438+521642, ZTF18aanbnjh	248.65767 52.27841	21.90±0.27	19.45±0.07	0.026	—	—	—	SN candidate	[11]
795202300001087	NSVS 5270259	247.70051 51.96916	13.84±0.01	12.99±0.01	0.022	957	3.03	0.674	EA	[1]
795203200009604	DDE 32	244.89910 52.77552	20.39±0.14	16.50±0.01	0.019	439	8.24	—	AM	[1]
795204100013041	ZTF18abgvctp	242.30742 52.21426	21.87±0.27	20.02±0.11	0.016	—	—	—	—	
795204200006882	CSS_J160450.1+520159	241.20883 52.03324	20.67±0.18	17.20±0.02	0.014	3909	4.20	316.8	EA	[1]
795205100007271	ZTF18aayatjf	252.30216 54.11178	21.45±0.23	19.51±0.08	0.021	—	—	—	—	
795205400001697	SDSS J164749.77+534217.3, ZTF18aajsmsrd	251.95740 53.70487	12.48±0.01	12.35±0.01	0.051	924	2.39	2.217	—	
795205400022890	IW Dra	251.56278 53.19847	14.69±0.01	11.57±0.01	0.047	4888	-1.99	193.2	Mira	[1]
795205400035251	SDSS J164533.41+531522.6	251.38937 53.25627	16.37±0.01	15.99±0.01	0.046	1353	5.21	230.3	—	
795209200003484	ZTF18abbpebf	251.54866 56.33124	21.33±0.22	18.96±0.05	0.015	—	—	—	—	
795209300012791	CSS_J164050.1+552654	250.20916 55.44835	16.27±0.01	15.17±0.01	0.015	5138	1.58	0.458	RRAB	[1]
795210400001565	SDSS J163331.55+554406.1	248.38139 55.73513	12.50±0.01	12.43±0.01	0.006	240	5.52	3.731	—	
795211200035931	SN 2018coi	244.74136 56.71714	20.35±0.15	18.04±0.03	0.009	—	-19.07	—	SN Ia	[12]
795212100007964	ZTF18aanbksq	242.93762 55.96133	21.72±0.27	19.28±0.07	0.007	—	—	—	—	

795213200000671	AT2018afr, Gaia18api, ZTF18aincjj	251.93077	58.50559	20.46±0.17	18.86±0.05	0.012	—	—	SN candidate	[1,3]
795213300001714	ASASSN-V J164454.40+573232.3	251.22667	57.54232	13.02±0.01	12.41±0.01	0.016	4974	-1.11	52.90	SR [1]
7952134000008053	NSVS J1647409+565803	251.91816	56.96779	14.98±0.01	13.25±0.01	0.017	8363	-1.40	111.3	SR [1]
7952143000016648		248.03423	57.75695	19.84±0.10	16.68±0.01	0.010	403	8.62	—	—
Disk										
807201100022915	V0476 Cas	25.84085	59.36414	15.93±0.01	12.79±0.01	0.512	3256	-1.11	227.1	Mira [1]
807202100027080	J022.6771+60.0173, ZTFJ013042.51+600102.4	22.67713	60.01735	16.61±0.01	15.44±0.01	0.441	1875	2.93	0.824	DBF, EA [2,3]
8072023000038681	MGAB-V574	20.22254	58.82538	20.74±0.22	17.24±0.02	0.474	2830	3.75	—	UG [1]
8072024000015654	V0420 Cas	22.80860	58.79127	14.82±0.01	13.72±0.01	0.419	2717	0.46	13.78	EA [1]
8072032000013118	J017.9869+59.7407, ZTF18abfyqzh	17.98693	59.74082	17.73±0.03	16.14±0.01	0.553	1026	4.65	2.185	—
8072033000044912	V0890 Cas	16.93576	59.05054	20.79±0.24	14.32±0.01	0.747	4536	-0.90	421.8	Mira [1]
8072034000031819	Romanov V28	19.30153	58.46788	19.28±0.08	16.09±0.01	0.414	1485	4.15	>20	UGSS [1]
8072034000037050	Dauban V254, ZTFJ011649.18+590500.2	19.20494	59.08340	16.74±0.02	14.17±0.01	0.491	2625	0.80	256.0	Mira [3]
807204200004799		14.29017	59.90208	20.19±0.17	18.05±0.03	0.435	4891	3.47	4.320	—
8072044000014494	ZTF18abhakel	16.16915	58.85506	14.88±0.01	13.86±0.01	0.607	1514	1.38	6.017	—
8072052000017536	V0367 Cas	25.29686	61.25982	16.30±0.01	13.48±0.01	0.964	1955	-0.48	3.709	EA [1]
8072062000003542	ASASSN-V J012356.42+615458.8	20.98505	61.91633	17.18±0.02	14.74±0.01	10.394	793	-21.81	—	VAR, YSO, PMS [1,4,5]
8072062000004116	MGAB-V1397	21.18448	61.89163	20.17±0.16	17.63±0.02	1.411	984	3.99	—	YSO, PMS [1,5]
8072062000014645	MGAB-V1388	20.49273	61.50519	18.45±0.04	16.28±0.01	0.887	935	4.11	—	YSO, PMS [1,5]
8072062000023036	NSVS J0122238+611352	20.59913	61.23097	16.53±0.01	12.84±0.01	0.626	4401	-2.01	325.1	Mira [1]
8072063000013468	II Cas	21.67063	60.77933	15.62±0.01	12.32±0.01	0.560	2997	-1.52	282.0	Mira [1]
8072064000014916	Mis V1358	22.34756	60.74668	17.36±0.02	12.92±0.01	0.489	2911	-0.67	310.0	Mira: [1]
8072071000005929	IRAS 01145+6132, ZTFJ011749.90+614805.9	19.45793	61.80168	17.80±0.03	14.25±0.01	1.013	3247	-0.95	278.0	LPV, Mira [3,6]
8072073000036103	BMAM-V362	16.98932	60.35615	20.46±0.18	17.79±0.03	0.540	2311	4.57	—	UGZ [1]
8072082000059506	V0450 Cas	12.87116	61.64957	16.42±0.01	13.93±0.01	1.223	560	2.01	—	INS [1]
8072083000012891	OU Cas	13.32034	60.69593	16.80±0.02	15.17±0.01	0.542	2434	1.82	1.265	EA [1]
8072083000016714	OT Cas	13.26166	60.59657	16.10±0.01	12.49±0.01	0.496	3145	-1.29	292.0	Mira [1]
8072084000015695	AV Cas	14.89163	60.72181	15.72±0.01	11.95±0.01	0.570	1695	-0.68	330.0	Mira [1]
8072084000036953	ZTF18abflqpt	14.44257	60.25802	20.01±0.14	17.48±0.02	0.445	2553	4.29	1.544	—
8072091000042420	Dauban V252, ZTFJ014817.58+630740.6	27.07326	63.12797	18.25±0.04	13.44±0.01	1.031	3624	-2.03	327.6	Mira [3]
8072093000012026	WISE J014237.7+623700	25.65734	62.61680	14.32±0.01	13.20±0.01	1.294	3020	-2.57	6.399	EA [1]
8072093000037143	NSVS J0141549+623406	25.47716	62.56828	16.89±0.02	12.32±0.01	1.349	4302	-4.36	297.0	Mira [1]
8072094000037670	IRAS 01438+6208	26.85197	62.38822	18.56±0.05	12.56±0.01	1.426	3518	-3.88	286.0	Mira [7]
8072101000028861	NSVS J0129109+631249, IRAS 01257+6257	22.29801	63.21435	16.28±0.01	12.70±0.01	1.357	5972	-4.71	454.2	LPV, SR+L, C [1,7]
807210200004045		21.24037	63.85572	19.48±0.09	17.84±0.03	1.550	3353	1.18	—	—
8072102000026027		21.96268	63.28808	18.81±0.06	16.56±0.01	1.451	1704	1.63	421.7	YSO, PMS, AGN [4,5,8]

807211100059466	V0724 Cas	18.72328 63.61240	15.55±0.01	12.54±0.01	1.488	5475	-5.03	280.0	Mira	[1]
807211300006190	Mis V0818, ZTFJ010441.96+625255.5	16.17487 62.88210	17.33±0.02	13.02±0.01	1.332	4768	-3.85	315.0	Mira	[3]
807211300012948	ZTFJ010526.59+624324.4	16.36079 62.72345	16.09±0.01	14.31±0.01	1.463	2785	-1.72	302.9	Mira	[3]
807211400009493	ZTF18abjcvcb	18.74697 62.83884	20.08±0.15	17.63±0.02	1.472	3334	1.18	2.546	—	
807212100012737	ZTF17aaeesd	15.01403 63.61420	19.01±0.07	16.51±0.01	1.196	1087	3.22	—	—	
807212100020830	ZTFJ005605.95+632426.8	14.02475 63.40745	16.80±0.02	13.26±0.01	1.016	3188	-1.90	394.4	Mira	[3]
807212200034055	[181] M 633	13.10185 63.06180	16.83±0.02	13.64±0.01	1.039	2171	-0.75	364.0	Mira	[9]
807212300038616	NSVS J0053173+623614, [181] M 644	13.32484 62.60320	19.61±0.11	14.55±0.01	1.306	3530	-1.59	311.0	L, Mira	[1,9]
807214100007080	[WVV2004] J0129273+653917	22.37209 65.65551	18.30±0.04	13.00±0.01	1.051	3655	-2.55	295.2	Mira	[7]
807214100026393	Dauban V269, ZTFJ012927.55+651147.8	22.36480 65.19663	20.94±0.27	16.75±0.02	1.074	3884	1.00	454.2	Mira	[3]
807214100042070	MGAB-V1402	24.06955 65.31108	20.11±0.16	18.24±0.04	1.125	3876	2.37	600.0	Mira	[1]
807214300010833	NSVS 1695145	21.24271 64.77038	16.53±0.01	13.84±0.01	1.315	4633	-2.91	560.0	Mira:	[1]
807214300051120	ZTFJ012430.53+641432.2	21.12717 64.24230	17.69±0.03	15.41±0.01	1.194	3852	-0.62	325.0	Mira	[3]
807215100019764	VSX J011759.4+652153	19.49756 65.36491	19.37±0.09	14.03±0.01	1.593	4243	-3.26	320.0	Mira:	[1]
807215200006611	NSVS J0108368+653701	17.15140 65.61674	16.78±0.02	12.71±0.01	1.580	5238	-5.00	309.0	Mira	[1]
807216100038423	IPHAS J005934.24+651815.1, ZTFJ005934.27+651814.9	14.89278 65.30412	18.25±0.04	14.47±0.01	1.412	2598	-1.27	295.2	AGB, Mira	[3,10]
807216200026731	NSV 15193	13.35496 65.03225	16.29±0.01	12.10±0.01	1.305	2681	-3.44	507.0	Mira	[1]
807216200045725	NSVS 1633482	11.72349 65.61549	21.30±0.34	15.52±0.01	1.411	3882	-1.10	390.0	Mira	[1]
807216400013229		14.15960 64.56684	17.41±0.02	16.29±0.01	1.381	2530	0.69	2.160	—	

† The best period extracted from either the Lomb–Scargle periodogram or one of the catalogues listed in the ZTF-viewer or determined by us.

* AM — AM Herculis-type variable

AGB — Asymptotic Giant Branch Star

C — Carbon star

DBF — Distant binary, full period

Delta Cep — Classical Cepheid

EA — β Persei-type (Algol) eclipsing system

INS — Orion variable with rapid light variations

L — Slow irregular variable, stars are often attributed to this type because of being insufficiently studied

LPV — Long Period Variable

Mira — α (omicron) Ceti-type variable

MSINE — Star showing modulated sinusoids

PNV — Possible nova

RRAB — RR Lyrae variable with asymmetric light curves

RSCVN — RS Canum Venaticorum-type binary system

RSg — Red supergiant

SN — Supernova

SR — Semi-regular variable

UG — U Geminorum-type variable, quite often called dwarf nova

UGSS — SS Cygni-type variable

UGZ — Z Camelopardalis-type star

VAR — Variable of unspecified type
 YSO — Young stellar Object of unspecified variable type

[1] — Watson et al. 2006; [2] — Heinze et al. 2018; [3] — Chen et al. 2020; [4] — Marton et al. 2016; [5] — Vroque et al. 2020; [6] — Usatov & Nosulchik 2008; [7] — Woźniak et al. 2004; [8] — Edelson & Malkan 2012; [9] — Nesci et al. 2018; [10] — Wright et al. 2009; [11] — Drake et al. 2009; [12] — Graham et al. 2018; [13] — Delgado et al. 2018; [14] — Massey et al. 2009; [15] — Carey 2017; [16] — Lee et al. 2014; [17] — Humphreys et al. 2017; [18] — Kodric et al. 2018; [19] — Magnier et al. 1997; [20] — Ovcharov et al. 2013; [21] — Shumkov et al. 2016; [22] — Hornoch & Kucakova 2015; [23] — Kodric et al. 2013; [24] — Joshi et al. 2003; [25] — Kaluzny et al. 1999.

REFERENCES

- Ahumada R., et al., 2020, *ApJS*, 249, 3
- Aleo P. D., et al., 2020, *Research Notes of the American Astronomical Society*, 4, 112
- Astropy Collaboration et al., 2013, *A&A*, 558, A33
- Astropy Collaboration et al., 2018, *AJ*, 156, 123
- Azimlu M., Marciniak R., Barmby P., 2011, *AJ*, 142, 139
- Bailer-Jones C. A. L., Rybizki J., Fouesneau M., Mantelet G., Andrae R., 2018, *AJ*, 156, 58
- Balanutsa P., et al., 2018, *The Astronomer's Telegram*, 11755, 1
- Ball N. M., Brunner R. J., 2010, *International Journal of Modern Physics D*, 19, 1049
- Baron D., Poznanski D., 2017, *MNRAS*, 465, 4530
- Bellm E. C., et al., 2019, *PASP*, 131, 018002
- Berdnikov L. N., Belinskii A. A., Shatskii N. I., Burlak M. A., Ikonnikova N. P., Mishin E. O., Cheryasov D. V., Zhuiko S. V., 2020, *Astronomy Reports*, 64, 310
- Berdygina S. V., 2005, *Living Reviews in Solar Physics*, 2, 8
- Berthier J., Vachier F., Thuillot W., Fernique P., Ochsenbein F., Genova F., Lainey V., Arlot J.-E., 2006, in Gabriel C., Arviset C., Ponz D., Enrique S., eds, *Astronomical Society of the Pacific Conference Series Vol. 351, Astronomical Data Analysis Software and Systems XV*. pp 367–+
- Blanton M. R., et al., 2017, *AJ*, 154, 28
- Boch T., Fernique P., 2014, in Manset N., Forshay P., eds, *Astronomical Society of the Pacific Conference Series Vol. 485, Astronomical Data Analysis Software and Systems XXIII*. p. 277
- Bonnarel F., et al., 2000, *A&AS*, 143, 33
- Borisov G., 2019, *IAU Minor Planet Center*, [MPEC 2019-R106](#), 1
- Boyajian T. S., et al., 2016, *MNRAS*, 457, 3988
- Breunig M. M., Kriegel H.-P., Ng R. T., Sander J., 2000, in *Proceedings of the 2000 ACM SIGMOD international conference on Management of data*. pp 93–104
- Cardamone C., et al., 2009, *MNRAS*, 399, 1191
- Cardelli J. A., Clayton G. C., Mathis J. S., 1989, *ApJ*, 345, 245
- Carey G., 2017, *Transient Name Server Discovery Report*, 2017-1418, 1
- Chambers K. C., et al., 2016, arXiv e-prints,
- Chen X., Wang S., Deng L., de Grijs R., Yang M., Tian H., 2020, *ApJS*, 249, 18
- Cristianini N., Shawe-Taylor J., et al., 2000, *An introduction to support vector machines and other kernel-based learning methods*. Cambridge university press
- D'Isanto A., Cavuoti S., Brescia M., Donalek C., Longo G., Riccio G., Djorgovski S. G., 2016, *MNRAS*, 457, 3119
- Delgado A., Harrison D., Hodgkin S., Leeuwen M. V., Rixon G., Yoldas A., 2018, *Transient Name Server Discovery Report*, 2018-345, 1
- Dick S. J., 2013, *Discovery and Classification in Astronomy: Controversy and Consensus*. Cambridge University Press, doi:10.1017/CBO9781139521499
- Drake A. J., et al., 2009, *ApJ*, 696, 870
- Edelson R., Malkan M., 2012, *ApJ*, 751, 52
- Filippenko A. V., 1992, in Filippenko A. V., ed., *Astronomical Society of the Pacific Conference Series Vol. 103, Robotic Telescopes in the 1990s*. pp 55–66
- Flewellling H. A., et al., 2016, arXiv e-prints,
- Förster F., et al., 2020, arXiv e-prints, p. arXiv:2008.03303
- France K., et al., 2013, *ApJ*, 763, 149
- Fukugita M., Ichikawa T., Gunn J. E., Doi M., Shimasaku K., Schneider D. P., 1996, *AJ*, 111, 1748
- Gaia Collaboration et al., 2018, *A&A*, 616, A1
- Giles D., Walkowicz L., 2019, *MNRAS*, 484, 834
- Giles D. K., Walkowicz L., 2020, *MNRAS*, 499, 524
- Ginsburg A., et al., 2019, *AJ*, 157, 98
- Graham M. L., et al., 2018, *The Astronomer's Telegram*, 11745, 1
- Guillochon J., Parrent J., Kelley L. Z., Margutti R., 2017, *ApJ*, 835, 64
- Guy J., et al., 2007, *A&A*, 466, 11
- Hastie T., Tibshirani R., Friedman J., 2009, *The elements of statistical learning: data mining, inference, and prediction*. Springer Science & Business Media
- Heinze A. N., et al., 2018, *The Astronomical Journal*, 156, 241
- Hornoch K., 2013, *The Astronomer's Telegram*, 5640, 1
- Hornoch K., Kucakova H., 2015, *The Astronomer's Telegram*, 7462, 1
- Hoyle B., Rau M. M., Paech K., Bonnett C., Seitz S., Weller J., 2015, *MNRAS*, 452, 4183
- Humphreys R. M., Gordon M. S., Martin J. C., Weis K., Hahn D., 2017, *ApJ*, 836, 64
- Hunter J. D., 2007, *Computing in Science and Engineering*, 9, 90
- Ishida E. E. O., 2019, *Nature Astronomy*, 3, 680
- Ishida E. E. O., et al., 2019, arXiv e-prints, p. arXiv:1909.13260
- Jayasinghe T., et al., 2020, *MNRAS*, 493, 4186
- Jolliffe I., 2013, *Principal Component Analysis*. Springer Series in Statistics, Springer New York, <https://books.google.fr/books?id=-ongBwAAQBAJ>
- Jones E., Oliphant T., Peterson P., et al., 2001, *SciPy: Open source scientific tools for Python*, <http://www.scipy.org/>
- Joshi Y. C., Pandey A. K., Narasimha D., Sagar R., Giraud-Héraud Y., 2003, *A&A*, 402, 113
- Kaluzny J., Mochejska B. J., Stanek K. Z., Krockenberger M., Sasselov D. D., Tonry J. L., Mateo M., 1999, *AJ*, 118, 346
- Kim D.-W., Protopapas P., Bailer-Jones C. A. L., Byun Y.-I., Chang S.-W., Marquette J.-B., Shin M.-S., 2014, *A&A*, 566, A43
- Klebesadel R. W., Strong I. B., Olson R. A., 1973, *ApJ*, 182, L85
- Kodric M., et al., 2013, *AJ*, 145, 106
- Kodric M., et al., 2018, *AJ*, 156, 130
- Kornilov M. V., Pruzhinskaya M. V., Malanchev K. L., Ishida E. E. O., Mondon F., Volnova A. A., Korolev V. S., 2019, in *The Multi-Messenger Astronomy: Gamma-Ray Bursts*. pp 100–110, doi:10.26119/SAO.2019.1.35517
- Lee C. H., et al., 2014, *ApJ*, 785, 11
- Liu F. T., Ting K. M., Zhou Z.-H., 2008, in *2008 Eighth IEEE International Conference on Data Mining*. pp 413–422
- Lochner M., Bassett B. A., 2020, arXiv e-prints, p. arXiv:2010.11202
- Lomb N. R., 1976, *Ap&SS*, 39, 447
- Magnier E. A., Augsteijn T., Prins S., van Paradijs J., Lewin W. H. G., 1997, *A&AS*, 126, 401
- Makarov D., Prugniel P., Terekhova N., Courtois H., Vauglin I., 2014, *A&A*, 570, A13
- Malanchev K., et al., 2020, in Elizarov A., Novikov B., Stupnikov S., eds, *Data Analytics and Management in Data Intensive Domains*. Springer International Publishing, Cham, pp 97–107
- Martínez-Galarza J. R., Bianco F., Crake D., Tirumala K., Mahabal A. A., Graham M. J., Giles D., 2020, arXiv e-prints, p. arXiv:2009.06760
- Marton G., Tóth L. V., Paladini R., Kun M., Zahorecz S., McGehee P., Kiss C., 2016, *MNRAS*, 458, 3479
- Masci F. J., et al., 2019, *PASP*, 131, 018003
- Massey P., Silva D. R., Levesque E. M., Plez B., Olsen K. A. G., Clayton G. C., Meynet G., Maeder A., 2009, *ApJ*, 703, 420
- Matheson T., et al., 2020, arXiv e-prints, p. arXiv:2011.12385
- McLachlan G. J., Peel D., 2000, *Finite mixture models*. Wiley Series in Probability and Statistics, New York
- Messier C., 1781, *Catalogue des Nébuleuses et des Amas d'Étoiles (Catalogue of Nebulae and Star Clusters)*, *Connaissance des Temps ou des Mouvements Célestes*
- Möller A., et al., 2020, arXiv e-prints, p. arXiv:2009.10185
- Mróz P., et al., 2020, *Research Notes of the American Astronomical Society*, 4, 13
- Narayan G., et al., 2018, *Astrophysical Journal, Supplement Series*, 236
- Nesci R., Tuvikene T., Rossi C., Gaudenzi S., Galletti S., Ochner P., Enke H., 2018, *Rev. Mex. Astron. Astrofis.*, 54, 341
- Norris R. P., 2017, *Publ. Astron. Soc. Australia*, 34, e007
- Nun I., Protopapas P., Sim B., Chen W., 2016, *AJ*, 152, 71
- Ovcharov E., et al., 2013, *The Astronomer's Telegram*, 5569, 1
- Pedregosa F., et al., 2011, *Journal of Machine Learning Research*, 12, 2825
- Penzias A. A., Wilson R. W., 1965, *ApJ*, 142, 419
- Perlmutter S., Muller R. A., Newberg H. J. M., Pennypacker C. R., Sasseen T. P., Smith C. K., 1992, in Filippenko A. V., ed., *Astronomical Society*

- of the Pacific Conference Series Vol. 103, Robotic Telescopes in the 1990s. pp 67–71
- Potantin S. A., Gorbunov I. A., Dodin A. V., Savvin A. D., Safonov B. S., Shatsky N. I., 2017, *Astronomy Reports*, **61**, 715
- Potantin S. A., et al., 2020, *Pisma v Astronomicheskii Zhurnal*, **46**, 895
- Press W. H., Teukolsky S. A., Vetterling W. T., Flannery B. P., 1992, Numerical recipes in C. The art of scientific computing
- Pruzhinskaya M. V., Malanchev K. L., Kornilov M. V., Ishida E. E. O., Mondon F., Volnova A. A., Korolev V. S., 2019, *MNRAS*, **489**, 3591
- Rebbapragada U., Protopapas P., Brodley C. E., Alcock C., 2009, arXiv e-prints, p. [arXiv:0905.3428](https://arxiv.org/abs/0905.3428)
- Reyes E., Estévez P. A., 2020, arXiv e-prints, p. [arXiv:2005.07779](https://arxiv.org/abs/2005.07779)
- Richardson D., Jenkins Robert L. I., Wright J., Maddox L., 2014, *AJ*, **147**, 118
- Richmond M., Treffers R. R., Filippenko A. V., 1993, *PASP*, **105**, 1164
- Ricker G. R., et al., 2014, in Space Telescopes and Instrumentation 2014: Optical, Infrared, and Millimeter Wave. p. 914320 ([arXiv:1406.0151](https://arxiv.org/abs/1406.0151)), [doi:10.1117/12.2063489](https://doi.org/10.1117/12.2063489)
- Samus' N. N., Kazarovets E. V., Durlevich O. V., Kireeva N. N., Pastukhova E. N., 2017, *Astronomy Reports*, **61**, 80
- Scargle J. D., 1982, *ApJ*, **263**, 835
- Schlafly E. F., Finkbeiner D. P., 2011, *ApJ*, **737**, 103
- Schölkopf B., Williamson R., Smola A., Shawe-Taylor J., Platt J., 1999. pp 582–588
- Segura A., Walkowicz L. M., Meadows V., Kasting J., Hawley S., 2010, *Astrobiology*, **10**, 751
- Shatsky N., et al., 2020, arXiv e-prints, p. [arXiv:2010.10850](https://arxiv.org/abs/2010.10850)
- Shumkov V., et al., 2016, *The Astronomer's Telegram*, **9470**, 1
- Skrutskie M. F., et al., 2006, *The Astronomical Journal*, **131**, 1163
- Solarz A., Bilicki M., Gromadzki M., Pollo A., Durkalec A., Wypych M., 2017, *A&A*, **606**, A39
- Soraisam M. D., et al., 2020, *ApJ*, **892**, 112
- Soraisam M. D., et al., 2021, *AJ*, **161**, 15
- Soszynski I., et al., 2008, *Acta Astron.*, **58**, 163
- Stetson P. B., 1996, *PASP*, **108**, 851
- Usatov M., Nosulchik A., 2008, *Open European Journal on Variable Stars*, **0087**, 1
- Valdes F., Gupta R., Rose J. A., Singh H. P., Bell D. J., 2004, *ApJS*, **152**, 251
- Villar V. A., et al., 2017, *ApJ*, **851**, L21
- Vioque M., Oudmajer R. D., Schreiner M., Mendigutía I., Baines D., Mowlavi N., Pérez-Martínez R., 2020, *A&A*, **638**, A21
- Voges W., et al., 1999, *A&A*, **349**, 389
- Watson C. L., Henden A. A., Price A., 2006, *Society for Astronomical Sciences Annual Symposium*, **25**, 47
- Webb S., et al., 2020, *MNRAS*, **498**, 3077
- Wenger M., et al., 2000, *A&AS*, **143**, 9
- Wes McKinney 2010, in Stéfan van der Walt Jarrod Millman eds, *Proceedings of the 9th Python in Science Conference*. pp 56 – 61, [doi:10.25080/Majora-92bf1922-00a](https://doi.org/10.25080/Majora-92bf1922-00a)
- Williams S. C., Hornoch K., Henze M., Darnley M. J., 2016, *The Astronomer's Telegram*, **9554**, 1
- Wilson O. C., 1968, *ApJ*, **153**, 221
- Woźniak P. R., Williams S. J., Vestrand W. T., Gupta V., 2004, *AJ*, **128**, 2965
- Wright N. J., Barlow M. J., Greimel R., Drew J. E., Matsuura M., Unruh Y. C., Zijlstra A. A., 2009, *MNRAS*, **400**, 1413
- Wright E. L., et al., 2010, *The Astronomical Journal*, **140**, 1868
- Wrzykowski L., et al., 2016, *The Astronomer's Telegram*, **9507**
- pandas development team T., 2020, *pandas-dev/pandas: Pandas*, [doi:10.5281/zenodo.3509134](https://doi.org/10.5281/zenodo.3509134), <https://doi.org/10.5281/zenodo.3509134>
- van der Walt S., Colbert S. C., Varoquaux G., 2011, *Computing in Science and Engineering*, **13**, 22

This paper has been typeset from a $\text{\TeX}/\text{\LaTeX}$ file prepared by the author.